Geosciences Faculty Articles   Geosciences

9-28-2023

Data-Driven Fuzzy Weights-Of-Evidence Model for Identification of Potential Zeolite-Bearing Environments on Mars

Gayantha R.L. Kodikara
University of Wisconsin-Milwaukee, gayantha_kodikara@yahoo.com

Lindsay J. McHenry
University of Wisconsin-Milwaukee

Follow this and additional works at: https://dc.uwm.edu/geosci_facart

Earth and Space Science

Data-Driven Fuzzy Weights-Of-Evidence Model for Identification of Potential Zeolite-Bearing Environments on Mars

Gayantha R. L. Kodikara[1] and **Lindsay J. McHenry**[1]

[1]Department of Geosciences, University of Wisconsin-Milwaukee, Milwaukee, WI, USA

Abstract The evolution of the climate and hydrochemistry of Mars is still a mystery but it must have been at least occasionally warm and wet to have formed the ancient fluvial and lacustrine landforms observed today. Terrestrial examples and geochemical modeling under proposed early Mars conditions show that zeolite minerals are likely to have formed under alkaline (pH > 8) conditions with low water/rock ratio and surface temperatures below 150°C. The identification and spatial association of zeolites on the surface of Mars could thus be used to reconstruct the paleoclimate, paleohydrochemistry, and geological evolution of some locations on Mars. Previous studies identified the zeolite analcime and discuss the difficulties of identifying other zeolite species on the surface of Mars using orbital spectroscopy. We used published global mineralogical, geological, geomorphological, hydrological, physical, and elemental abundance maps and the locations of hydrous minerals detected and mapped using orbital data to create a map that delineates favorable areas to look for zeolites on Mars. We used the data-driven fuzzy-based Weights-of-Evidence method to identify and map favorable areas for zeolites on the surface of Mars up to ±40° latitude toward the poles. The final map shows that the eastern and western Arabia deposits, some sites in the Medusae Fossae formation, and some areas within and near Valles Marineris, Mawrth Vallis, highlands north of Hellas, and the Terra Cimmeria and Terra Sirenum regions would be favorable areas to look for zeolites using targeted orbital spectral analysis or future in situ observations.

Plain Language Summary Our knowledge of early Mars environmental conditions is limited. Field examples from the Earth and computer models that simulate how zeolites form under early martian conditions showed that they prefer water-limited, high pH conditions and surface temperatures below 150°C. Therefore, if zeolite minerals are present in certain locations on the surface of Mars, based on their presence, we can infer the geological and environmental history of that location. We used a computer model to identify where zeolite minerals can be present on Mars, based on existing maps and data sets of martian surface features, properties, and compositions. Using that model, we identified several areas of Mars that would have been favorable for zeolites, which could be targeted for future more detailed studies.

1. Introduction

Zeolites are some of the most common authigenic silicate minerals in terrestrial sedimentary deposits (Hay, 1966; Hay & Sheppard, 2001). Zeolite occurrences in sedimentary environments on Earth can be categorized into six groups based on their geologic and hydrologic settings; (a) saline-alkaline lakes (e.g., Lake Tecopa, California; Sheppard & Gude, 1968), (b) soils and land surfaces (e.g., Lake Bogoria basin, Kenya; Renaut, 1993), (c) deep sea sediments (e.g., North-West Pacific; Lee, 1988), (d) open hydrologic systems (e.g., the White River sequence, Wyoming, USA; Lander & Hay, 1993), (e) hydrothermal alteration (e.g., Yucca Mountain, Nevada, USA; Sheppard et al., 1988), and (f) burial diagenesis (e.g., Mogami district, Yamagata, Japan; Iijima, 1988). Overall, zeolites are most abundant in volcaniclastic deposits since volcanic glass is a major zeolite precursor (Hay & Sheppard, 2001). Whether zeolites form and are preserved depends on the thermodynamic equilibrium of fluid-mineral reactions caused by water chemistry (Chipera & Apps, 2001), and kinetically controlled non-equilibrium growth and dissolution reactions (Dibble & Tiller, 1981). Therefore, the presence and nature of zeolites is a good probe to reconstruct the geological and hydrological history of zeolite-bearing environments on Earth (e.g., Chipera & Apps, 2001; McHenry et al., 2020).

Zeolites are also postulated as components of the martian regolith (e.g., Basu et al., 1998; Berkley & Drake, 1981; Bish et al., 2003; Cannon et al., 2015; Dickinson & Rosen, 2003; Ming & Gooding, 1988; Tokano & Bish, 2005).

Geochemical modeling shows that zeolites on early Mars are likely to have formed under alkaline (pH > 8) conditions with low water/rock ratios and surface temperatures below 150°C (e.g., Kodikara, McHenry, & Grundl, 2023; Semprich et al., 2019; Zolotov & Mironenko, 2016). Since the hydrochemistry and climate of early Mars remain a mystery, identifying and mapping zeolites on the surface of Mars can be used to reconstruct not only the paleoclimate and paleohydrochemistry, but also the geological evolution of Mars. Ehlmann et al. (2009) detected analcime in craters near Antoniadi basin, west of Nili Fossae, using Compact Reconnaissance Imaging Spectrometer for Mars (CRISM) orbital data. Carter et al. (2013) conducted a large-scale investigation of hydrous minerals on Mars using CRISM and OMEGA (Observatoire pour la Mineralogie, l'Eau, la Glace et l'Activite) orbital imaging spectrometer data. They categorized zeolites and sulfates into one class due to the difficulty of distinguishing them using orbital data, though they typically form in very different environments. However, based on the shape of the 1.9 μm absorption band, they infer that more than 80% of minerals assigned to that class are likely zeolites. Sun and Milliken (2015) conducted a survey to identify hydrous minerals in 633 crater central peaks using CRISM data and only identified zeolites in 4.5% of them. These studies along with the laboratory (e.g., Kodikara et al., 2022) and earth analog orbital remote sensing (e.g., Kodikara, McHenry, van der, & Meer, 2023) studies emphasized the difficulty of identifying non-analcime zeolites using Visible-near Infrared—Shortwave Infrared (VNIR-SWIR) spectral data. Zeolites have also not yet been reported from in situ observations on Mars or in martian meteorites.

Therefore, the identification and delineation of prospective areas for zeolites on the surface of Mars could serve as a guide for further searches for zeolites using detailed orbital spectral image analysis and future in situ observations. Predictive modeling for mineral exploration, a widely used statistical and probabilistic reasoning method in geosciences, can be used in this case (Bonham-Carter et al., 1989; Pan & Harris, 2000). Predictive modeling for mineral exploration follows specific steps and starts by defining a conceptual model for the exploration target. To define a conceptual model for exploration targets for the mineral type of interest (zeolite in this case) requires knowledge of the possible geological and geochemical formation processes of the target mineral. This knowledge allows exploration criteria to be defined, followed by the selection of suitable geoscience spatial data sets to be used, the extraction and enhancement of prospective features in each data set, selecting mapping method(s) for each prospective feature, selecting method(s) for creating predictive map(s) from each prospective feature, and then integrating the predictive maps to create a predictive model and/or to map the prospective areas for the target mineral (zeolites) (Bonham-Carter et al., 1989; Carranza, 2011). The preferred predictive model for this study should (a) accommodate the multiclass and continuous geodata, and (b) be sufficiently robust to handle the "information fuzziness" inherent to remote observational data (Porwal et al., 2003; Zimmermann, 1991). The combination of the Weights-of-Evidence (WEM) method and fuzzy set theory can fulfill both criteria flexibly and consistently.

The WEM method is commonly applied for mineral exploration, landslide susceptibility analysis, and hazard modeling (e.g., Bonham-Carter, 1994; Bonham-Carter et al., 1989; Neuhäuser & Terhorst, 2007). It has also been used for habitat quality assessments (e.g., Romero-Calcerrada & Luque, 2006), and even mapping the potential habitat of underground mushrooms (Yang et al., 2012). To map the potential mineral deposits, the model uses the location of known mineral occurrences to identify the favorable geological and environmental factors that can help map the potential distribution of the desired mineral (Bonham-Carter et al., 1989). Fuzzy set theory is also used for predictive mineral potential mapping since it provides a mathematical framework for combining and analyzing quantitative and qualitative data independent of their characteristics or source (X. Luo & Dimitrakopoulos, 2003; Moon, 1998; Porwal et al., 2003). Cheng and Agterberg (1999) proposed a hybrid fuzzy WEM, in which subjective or objective definitions of a fuzzy membership function of evidence can be supplemented by a more objective WEM-calculated definition of conditional probabilities. Due to our limited knowledge of the formation conditions (geological, mineralogical, physical, and hydrological) of zeolites on Mars, a data-driven (empirical) approach was used. Data-driven methods typically assume that a sufficient number of known zeolite occurrences within the study area have been well studied and documented (Porwal et al., 2003). Since there are no well-studied and documented zeolite detections on Mars, this study first models the favorable areas for hydrous minerals and based on that model identifies the favorable areas for zeolites using other information and assumptions.

The conceptual model developed in this study requires: (a) the suitable geologic and hydrologic environments for the formation of hydrous minerals, which are commonly formed under lacustrine, hydrothermal, diagenesis/metamorphic, or pedogenic processes, and (b) the presence of volcanic ash (tuff) as a starting material for the

formation of zeolites. Therefore, as a first step, this study creates a predictive model (map) for the potential areas for hydrous minerals on Mars, and then based on the available information and models of distribution of pyroclastic ash deposits of Mars, creates a predictive model (map) for the most likely areas for zeolites on the surface of Mars.

2. Data Sets

Data sets for this study were selected based on the spatial association of zeolites with other chemical, mineralogical, geological, and geomorphological factors observed in the Earth's zeolite bearing environments.

2.1. Hydrous Mineral Map

Zeolite minerals are mostly associated with other hydrous minerals and therefore the presence of certain hydrous minerals can be used not only to predict the presence of zeolite, but also the zeolite alteration pattern (e.g., Kodikara & McHenry, 2021). Carter et al. (2013) conducted a global survey of martian hydrous minerals using CRISM and OMEGA hyperspectral data and sorted their hydrous detections into nine classes of spectra: (a) Fe/ Mg - phyllosilicates, (b) chlorites, (c) Al-smectites/micas, (d) Al-rich kaolins, (e) opaline silica, (f) zeolites/ sulfates, (g) serpentines/carbonates, (h) prehnite, and (i) epidote. The database of detected hydrous mineral locations by Carter et al. (2013) was downloaded from https://www.cosmos.esa.int/web/psa/mars-maps.

2.2. Geology

The geologic maps provide unique information on the spatial and temporal sequences of geological processes on the surface of the planet. Formation and presence of zeolites in a certain location is based on the geologic and hydrologic processes that occurred in that location during a certain period. Therefore, geology maps will be a great help to find the suitable areas to form and find zeolites. Tanaka, Robbins, et al. (2014) and Tanaka, Skinner, et al. (2014) applied photogeologic mapping techniques to map 44 geologic units and 13 linear feature types, categorizing units on the surface based on the timing of major episodes and the types of materials involved (Tanaka, Robbins, et al., 2014; Tanaka, Skinner, et al., 2014). The geology map, created by Tanaka, Robbins, et al. (2014) and Tanaka, Skinner, et al. (2014) was downloaded from https://pubs.usgs.gov/sim/3292/.

2.3. Elemental Abundances

The water-equivalent hydrogen calculated from neutron data is used to predict the presence and distribution of zeolites and other hydrous minerals on Mars (e.g., Fialips et al., 2005; Mitrofanov et al., 2022). Ojha et al. (2021) used the K and Th enriched regions on Mars, calculated from the Gamma Ray Spectrometer (GRS) on the 2001 Mars Odyssey Mission (Boynton et al., 2004), to find potential hydrothermal systems on Mars. Hydrothermal systems are one of the main zeolite forming environments on the Earth (Hay & Sheppard, 2001), and also proposed for Mars (e.g., Ehlmann et al., 2009). Poulet et al. (2007) mapped H, Si, Cl, K, and Th concentrations measured by the GRS for $\pm \sim 45°$ latitudes assuming that all elements are homogeneous in the top few tens of centimeters of surface materials. For this study, two map products by Poulet et al. (2007), $2° \times 2°$ and $5° \times 5°$ binned point data, were downloaded from https://grspds.lpl.arizona.edu.

2.4. Mineralogy

Mineral association is used as one of the key ways to find a target mineral in mineral exploration. The presence of certain minerals (e.g., K-feldspar), as well as the absence of certain minerals (e.g., olivine), can be used as an evidential factor to predict the presence (or absence) of zeolite in that location. Bandfield (2002) produced a global mineral distribution map using data from the Thermal Emission Spectrometer (TES) on the Mars Global Surveyor (MGS) spacecraft (Christensen et al., 1992). The global mineral concentration maps include (a) sheet silicates and high-Si glass, (b) sulfate, (c) plagioclase, (d) hematite, (e) carbonate, (f) K-feldspar, (g) basaltic glass, (h) quartz, (i) High-Ca pyroxene, (j) low-Ca pyroxene, (k) olivine, and (l) amphibole. Mineral concentrations were calculated based on signal strength relative to the mineral endmembers used in the linear spectral deconvolution method.

Poulet et al. (2007) produced maps of the global distribution of martian surface material based on the data from one martian year of OMEGA observations. Global maps of hydrated minerals, mafic minerals, and ferric phases were derived using spectral parameters. Ody et al. (2012) produced maps detailing the global distribution of these mineral species using the entire OMEGA data set acquired from January 2004 to August 2010, when the 1–2.5 μm channel cooler failed. Since the 1–2.5 μm regions are important to discriminate most martian mineralogy, these global maps can be considered the final outcome of OMEGA observations (Ody et al., 2012).

The global mineral abundance maps derived both from TES by Bandfield (2002) and from OMEGA by Ody et al. (2012) were downloaded from https://www.cosmos.esa.int/web/psa/mars-maps.

2.5. Albedo

Observations of the surface albedo of Mars show significant changes over time, likely due to global dust storms that redistribute dust (Pleskot & Miner, 1981; Putzig & Mellon, 2007). High-Si glass, a common precursor of zeolites, shows its highest concentrations in northern low albedo regions, while the high albedo regions are interpreted as covered by anhydrous ferric oxides (Bandfield, 2002). The albedo map is also used to compare and interpret the other spectral parameters (e.g., Poulet et al., 2007). A NIR (Near Infrared) 1 μm albedo (lambertian albedo) map produced by Ody et al. (2012) using the I/F/cos(i) value at 1.08 μm (where i = solar incident angle) of OMEGA data from January 2004 to August 2010 was used for this study. The TES bolometric albedo global map with 8 pixels per degree (ppd, 7.5 km) spatial resolution (Christensen et al., 2001) was also used.

2.6. Thermal Inertia

The thermal inertia of a certain location on Mars is typically consistent with properties including the abundance of rocks, particle size, extent of bedrock exposure, degree of induration, and how these properties are combined within the field of view (Mellon et al., 2000). The spatial variation of thermal inertia can reflect the physical characteristics and the processes that formed/modified the martian surface. Though there is no direct relation between the presence/formation of zeolites and thermal inertia, based on our current knowledge, it will be interesting to find if there is any statistical correlation between them for further studies. Putzig and Mellon (2007) have produced nighttime and daytime seasonal maps of apparent thermal inertia using 3 years of TES data at 20 ppd (3 km). They have cropped each of the 36 seasonal maps latitudinally and used the median values to create daytime and nighttime thermal inertia maps. These two maps were downloaded from https://www.mars.asu.edu/data/.

2.7. Dust Cover

Ruff (2004) shows spectral evidence for zeolites in the dust on Mars using TES data, though it is uncertain (e.g., Bandfield et al., 2003). However, the spatial distribution of dust cover is also important for remote sensing studies since it may mask the spectral signatures of the surface materials. Ruff and Christensen (2002) introduced a dust cover index (DCI) defined by the average emissivity value in the wavelength region from 1,350 to 1,400 cm^{-1}. They have produced a DCI map using nadir-pointing, daytime TES spectral data with brightness temperature >260 K. The TES were binned at 8 ppd (7.5 km pixel resolution), with any gaps filled using linear interpolation. This DCI map was downloaded from http://www.mars.asu.edu/~ruff/DCI/dci.html.

The dust index map derived from TES by Bandfield (2002) using the linear spectral deconvolution method was also used. The dust index maps show a remarkable spatial coherence with albedo and thermal inertia maps at many scales. Dust free surfaces have very low albedo. However, thermal inertia is not well-suited for this due to its complex behavior for mixtures of dust and coarse particles (Ruff & Christensen, 2002).

2.8. Elevation and Slope

Elevation information of planetary surfaces is used to derive the morphology of the surface to analyze landscape forms, processes, patterns, and evolution (Schumm, 1991). This morphological information is also important for locating low-lying places where water might accumulate at local (e.g., basins) and global (e.g., northern lowland area) scales, and other places where zeolites are commonly formed, such as canyons, crater central peaks, etc.

The elevation and slope maps were derived from the 463 m/pixel resolution of digital elevation data (DEM) from Mars Orbiter Laser Altimeter (MOLA) on MGS (Smith et al., 2001). The MOLA DEM data was downloaded from https://astrogeology.usgs.gov.

2.9. Valley Networks

Zeolite deposits on the Earth can be classified into two main groups, those formed in open hydrologic systems or closed hydrologic systems. Zeolite deposits in open hydrologic systems on the Earth are often several hundred meters thick and can be traced laterally for tens of kilometers, and typically form due to flowing or percolating groundwater through valley networks (Sheppard & Hay, 2001). Several global valley network maps on Mars have been produced both manually from Viking data (Carr & Chuang, 1997), MOLA and Thermal Emission Imaging System (THEMIS) data (Hynek et al., 2010), and THEMIS, Context Camera (CTX), and MOLA data (Alemanno et al., 2018), and automated mapping using MOLA data (W. Luo & Stepinski, 2009). The global valley network map produced by Alemanno et al. (2018) was used in this study. Mapping classes include (a) valley networks, (b) longitudinal valleys, (c) valleys on volcanoes, (d) valleys adjacent to canyons, (e) single valleys and valley segments, and (f) small outflow channels. The global geologic map of Mars, created by Tanaka, Robbins, et al. (2014) and Tanaka, Skinner, et al. (2014), included three classes of valleys, (a) single valley, (b) small outflow valley, and (c) trough fluvial valley. These segment maps were used in this study.

2.10. Open and Closed Basins

Zeolite deposits are mostly found in present and paleo saline, alkaline lakes on the Earth. Several geochemical modeling studies show a high possibility of forming zeolites in ancient lakes on Mars (e.g., Kodikara, McHenry, & Grundl, 2023; Zolotov & Mironenko, 2016). Possible paleolake basins observed on Mars have been cataloged and categorized into two main groups based on their morphological features: (a) Closed-basin lakes with an inlet valley and no outlet valley, and (b) Open-basin lakes having inlet valleys and outlet valleys (Cabrol & Grin, 1999; Fassett & Head, 2008; Goudge et al., 2012, 2015, 2016). For this study, the open and closed-basin lakes catalog compiled by Goudge et al. (2016) was used. The database consists of the locations of 205 closed-basin lakes (Goudge et al., 2015) and 220 open-basin lakes (Fassett & Head, 2008; Goudge et al., 2012). However, this database does not contain potential paleolakes without inlet valleys (like Columbus crater; Wray et al., 2011), possibly fed by groundwater (e.g., Boatwright & Head, 2021, 2022; Hargitai et al., 2018; Wray et al., 2011). This type of paleolake may have also been common on early Mars.

2.11. Pyroclastic Deposits

Basaltic or silicic glass from volcanic ash, tephra, pyroclastic flows, or detrital grains from lava flows are the major precursor material of zeolite (Hay, 1966). Explosive volcanic eruptions were likely frequent during the Noachian and Hesperian periods (Wilson & Head, 2007). This study uses a map of deposits identified in the literature as potentially pyroclastic that are larger than 10^5 km^2 (Broz et al., 2020; Kerber et al., 2012; Tanaka, 2000). The mapped deposits include Arabia deposits, Electris deposits, Medusae Fossae Formation (MFF), Dorsa Argentea Formation, Hellas deposits, Argyre deposits, Tyrrhena Patera deposits, and Isidis deposits.

Kerber et al. (2013) simulated ancient martian explosive eruptions (assuming a range of higher atmospheric pressures: 50 mbar, 0.5 bar, 1 bar, and 2 bar) using a planetary global circulation model developed by the Laboratoire de Meteorologie Dynamique (LMD). Most martian explosive volcanic centers date to the Hesperian, which likely had higher atmospheric pressure than at present (e.g., Ramirez, 2017). The particle size used for their simulation was 35 μm in radius representing small, far-field ash. For this study, a combined ash distribution pattern map created by Kerber et al. (2013) from all major martian volcanic centers, assuming each erupted 1.4×10^6 km^3 of ash during their lifetimes under 1 bar of pressure, was selected.

3. Methods

3.1. Preparation of Factor Maps

All the factor maps discussed above were imported into ILWIS (ILWIS, 2005) via GDAL (GDAL/ORG contributors, 2020) and ISIS3 (Adoram-Kershner et al., 2020). All analysis was done using ILWIS (running on Linux
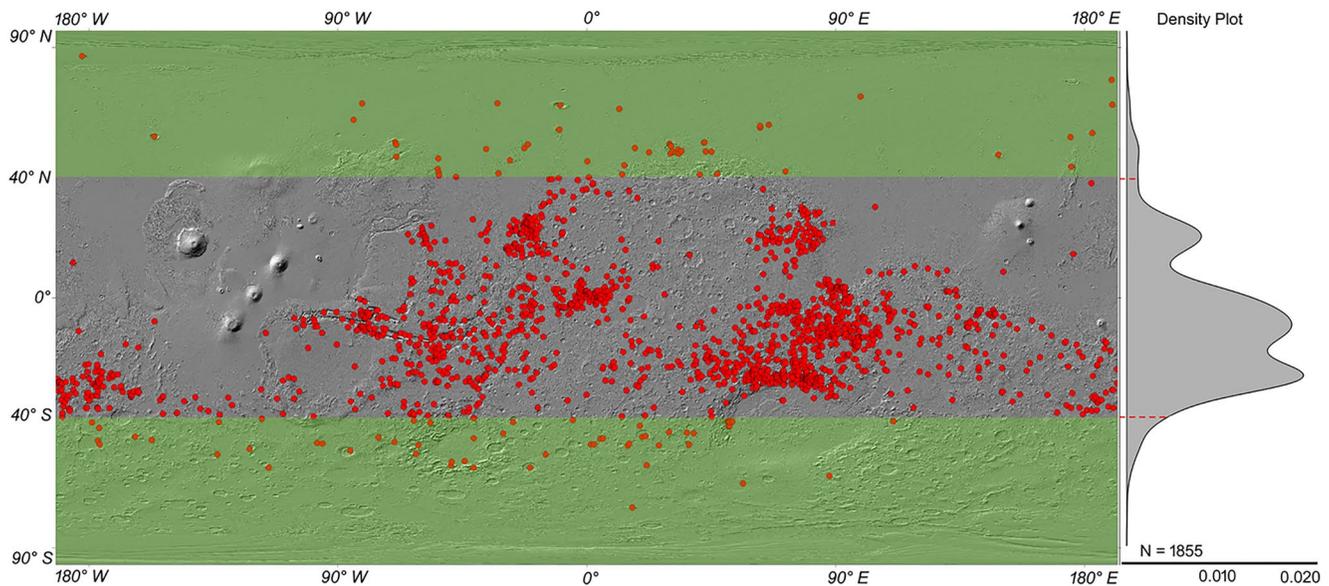
Figure 1. Map of hydrous mineral detections on Mars. Each point represents the location of a hydrous mineral detection by Compact Reconnaissance Imaging Spectrometer for Mars and/or OMEGA. Background is a grayscale hillshade map created from Mars Orbiter Laser Altimeter DEM. Point density plot shows on the left side of the map.

Pop-OS), followed by re-projecting to a common coordinate system (Plate Carree projection system), and resampling into 200 m/pixel resolution using the nearest neighbor method.

Total hydrous mineral locations detected by Carter et al. (2013) are shown in Figure 1. The abundance of those hydrous mineral detections along with the latitudes are shown in the density plot in Figure 1. This shows that more than 90% of the total detections (1,735/1,855) are in the area between latitudes 40°N and 40°S. Since the importance of the map classes/area are calculated based on the locations of hydrous mineral detections, the limited detections in the area beyond 40°N and 40°S latitudes will be less important. Therefore, to reduce the computational power, time, and memory space, sub maps were created from all the factor maps covering the area between latitudes 40°N and 40°S for the rest of the work.

All the continuous data raster maps (e.g., elevation, dust cover index, elemental abundance, etc.) were reclassified into 10 classes after careful examination of the histograms of the pixel values and based on the discussions in the corresponding literature. The discontinuous data raster maps (categorical maps, e.g., geology map) were imported as is. The 10 buffer regions (A: 0–200 m, B: 200–400 m, C: 400–600 m, D: 600–800 m, E: 800–1,000 m, F: 1,000–2,500 m, G: 2,500–5,000 m, H: 5,000–10,000 m, I: 10,000–100,000 m, and J: >100,000 m) were created from the segment maps and then rasterized. Based on the spatial association of buffer regions with the hydrous mineral detections, three buffer maps were selected. The boundaries of all the possible closed and open-basin lakes were manually digitized with the help of MOLA DEM. Two binary maps were created from the ash deposits map (ash deposit = 1, other area = 0) and open and closed paleolake basin map (open/closed basins = 1, other area = 0).

The total hydrous mineral detections within the sub map area (1,735 points) were divided into two classes (train and test) using the stratified random sampling method. The H_2O weight percentages at each point location were extracted from the H_2O GRS map for the stratified random sampling method assuming that hydrous mineral abundances at each point location can be represented by the GRS H_2O map. Data partitioning was done using "caret" package in R. The train point map contains ~80% (1,391 points) of the total points, while the test point map contains the rest of the data points (~20%, 344 points). The factor maps used in this study are listed in Table 1, and each factor map is referred to using the MapID throughout the rest of the text.

3.2. Weights-of-Evidence (WEM)

The WEM was originally developed in the field of quantitative medical diagnosis and later used in the prediction of mineral deposits by Bonham-Carter et al. (1989). This empirical approach can calculate the relative

Table 1
Factor Maps Used in This Study

Number	Platform	Product	MapID	References
		RASTER		
1	OMEGA	NIR albedo	om_albdo	Ody et al. (2012)
2		Fe^{3+}	om_fe530	
3		$nphsFe^{3+}$	om_nnphs	
4		Pyroxene	om_pyrox	
5		Olivine Spectral Parameter1	om_osp1m	
6		Olivine Spectral Parameter2	om_osp2m	
7		Olivine Spectral Parameter2	om_osp2m	
8	TES	Albedo	ts_albdo	
9		Amphibole	ts_amphi	Bandfield (2002)
10		Carbonate	ts_carbo	
11		High Calcium Pyroxene	ts_hcpmp	
12		Low Calcium Pyroxene	ts_lcpmp	
13		Hematite	ts_hemat	
14		K-feldspar	ts_kfeld	
15		Olivine	ts_olvne	
16		Plagioclase	ts_plgcl	
17		Quartz	ts_quatz	
18		Sulfate	ts_sulft	
19		Dust	ts_dustm	
20		Dust Cover Index (DCI)	ts_dcimp	Ruff and Christensen (2002)
21		Thermal Inertia-Day	ts_tiday	Putzig and Mellon (2007)
22		Thermal Inertia-Night	ts_tingt	
23	GRS	H_2O	gr_h2omp	Boynton et al. (2007)
24		Si	gr_simap	
25		K	gr_kmaps	
26		Cl	gr_clmap	
27		Fe	gr_femap	
28		Th	gr_thmap	
29	VIKING	Global Mosaic 232 m v2	vk_color	USGS Astrogeology
30	MGS	MOLA DEM	mg_mldem	Smith et al. (2001)
31		Hilshade map from MOLA	mg_hilsd	
32		Slope map from MOLA	mg_slope	
		VECTOR		
33		Geology Map of Mars 2014	tn_geolo	Tanaka, Robbins, et al. (2014) and Tanaka, Skinner, et al. (2014)
34		Hydrous mineral map	ct_hydst	Carter et al. (2013)
35		Open-closed basins	tg_basin	Goudge et al. (2016)
36		Valley Network	ga_vlnet	Alemanno et al. (2018)
37		Long Valley	ga_logvl	Alemanno et al. (2018)
38		Trough Fluvial	tn_trflu	Tanaka, Robbins, et al. (2014) and Tanaka, Skinner, et al. (2014)
39		Pyroclastic ash distribution	lk_pyash	Kerber et al. (2013)
40		Pyroclastic deposits	pb_pydep	Broz et al. (2020)

A = Ash deposits

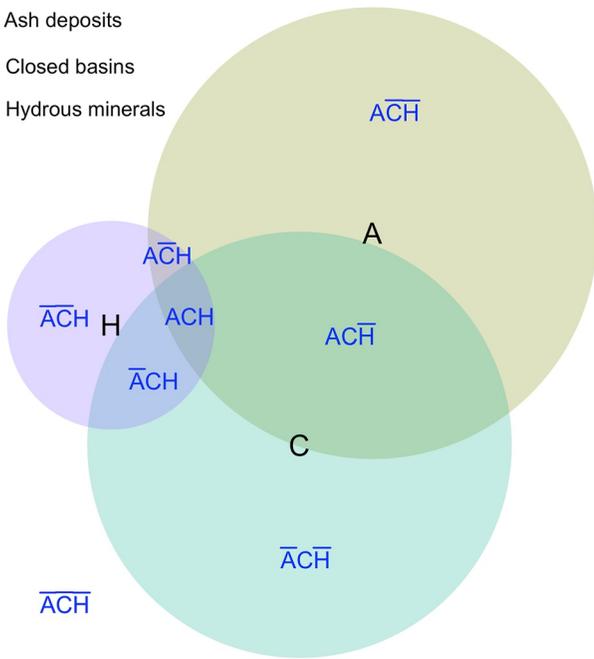C = Closed basins

H = Hydrous minerals

Figure 2. Venn diagram for the relations between binary patterns.

importance of individual evidence maps using statistical methods (Bayesian relation) assuming that all variables are conditionally independent of mineral occurrences (Pan & Harris, 2000). For simplicity, the integration of two explanatory binary maps by WEM will be discussed. The two explanatory indicator maps, the pyroclastic ash deposits map and closed basins map, are denoted by A and C, respectively. The single target indicator variable, in this case the location map of detected hydrous minerals, is indicated by H. These maps are regarded as random variables that are either present or absent (binary) in a unit cell. The possible relations between C, A, and H are shown in Figure 2 Venn diagram. $\overline{A}$, $\overline{C}$, and $\overline{H}$ represent the absence status of A, C, and H, respectively.

The prior probability $P\{H\}$ is the probability of the occurrence of hydrous minerals in the entire study area, which can be calculated using the ratio of detected hydrous mineral pixels (or area), H to the total number of pixels in the study area (or total area), T.

$$p(H) = \frac{H}{T} \tag{1}$$

The relations between A, C, and H can be expressed by eight probabilities based on the assumption of conditional independence (CI) between A and C with respect to H.

$$p(ACH), p\left(AC\overline{H}\right), p\left(A\overline{C}H\right), p\left(\overline{A}CH\right), p\left(\overline{A}\overline{C}H\right), p\left(\overline{A}C\overline{H}\right), p\left(A\overline{C}\overline{H}\right), p\left(\overline{A}\overline{C}\overline{H}\right)$$

These eight probabilities are mutually related by

$$p(ACH) = p(A|H)p(C|H)p(H) \tag{2}$$

$$p\left(AC\overline{H}\right) = p\left(A|\overline{H}\right)p\left(C|\overline{H}\right)p\left(\overline{H}\right) \tag{3}$$

Based on the above relations, four conditional probabilities (posterior probabilities) can be calculated. As an example,

$$p\frac{(A)}{(H)} = \frac{p(A) \times p(H/A)}{p(H)} \tag{4}$$

where H is the occurrence of hydrous minerals, A is the pyroclastic deposits map, and $p(H/A)$ is the conditional probability of having hydrous minerals in the area where pyroclastic deposits are present.

Four weights, W_A^+, W_A^-, W_C^+, and W_C^-, can be calculated for each evidence class and these weights are dependent on the spatial relationship between the potential occurrence of hydrous minerals and the selected evidence map.

$$W_A^+ = ln\left\{p(A|H)/p\left(A|\overline{H}\right)\right\}, W_A^- = ln\left\{p\left(\overline{A}|H\right)/p\left(\overline{A}|\overline{H}\right)\right\} \tag{5}$$

$$W_C^+ = ln\left\{p(C|H)/p\left(C|\overline{H}\right)\right\}, W_C^- = ln\left\{p\left(\overline{C}|H\right)/p\left(\overline{C}|\overline{H}\right)\right\} \tag{6}$$

W^+ in each evidential map indicates the importance of the presence of the factor class for the occurrence of hydrous minerals. Positive W^+ values for a factor class indicate its favorability for the occurrence of hydrous minerals, while negative W^+ values denote unfavorability. W^- is used to evaluate the importance of the absence of a factor class for the occurrence of hydrous minerals. If W^- is positive, it indicates that the absence of the factor class makes the area more favorable for the occurrence of hydrous minerals. If W^- is negative, the absence of the factor class is unfavorable. Zero weights do not show a correlation between the factor class and hydrous mineral occurrences.

The contrast ($C = W^+ - W^-$) represents the strength of association between the explanatory map (e.g., pyroclastic deposit map, A) and the target map (e.g., detected hydrous mineral location map, H). Large contrast values imply

Table 2
Slope "a" Values Used in Logistic Membership Functions (Equations 8 and 11)

Map 1–10	a	Map 11–20	a	Map 21–30	a
fzm_gr_femap	1	fzm_ts_kfeld	1	fzm_gr_h2omp	3
fzm_gr_kmaps	1	fzm_ts_olvne	1	fzm_om_fe530	4
fzm_om_osp1m	1	fzm_ts_plgcl	1	fzm_om_nnphs	4
fzm_om_osp2m	1	fzm_ts_sulft	1	fzm_tn_geomp	5
fzm_om_osp3m	1	fzm_gr_simap	2	fzm_gr_clmap	5
fzm_om_pyrox	1	fzm_gr_thmap	2	fzm_mg_mldem	5
fzm_ts_amphi	1	fzm_ts_carbo	2	fzm_om_albdo	5
fzm_ts_hcpmp	1	fzm_ts_quatz	2	fzm_ts_albdo	5
fzm_ts_lcpmp	1	fzm_ts_tiday	2	fzm_ts_dcimp	5
fzm_ts_hemat	1	fzm_ts_tingt	2	fzm_ts_dustm	5

strong association between two factors while small contrast values indicate the opposite. The studentized contrast (C_{std}, also called the normalized contrast) is defined as the ratio of C to its standard deviation ($S(C)$) and is used as an indicator of confidence.

$$C_{std} = \frac{C}{\sqrt{S^2(W^+) + S^2(W^-)}} \tag{7}$$

where, $S^2(W^+)$ and $S^2(W^-)$ are the variances of W^+ and W^-, respectively.

The hydrous mineral training points (1,391 points) were used to calculate the weight values (W^+, W^-), C, and C_{std} for each class in each map. Based on the weights and C_{std}, the study proceeded with the 30 selected factor maps (Table 2). These maps are spatially highly correlated (positively and negatively) with the hydrous mineral detections.

3.3. Fuzzy Set Theory

Most tools used for formal reasoning, modeling, and computing are deterministic, precise, and crisp. They are yes-or-no types rather than greater-or-less types. As an example, zeolite is present (or not) in a closed basin of Mars, instead of greater possibility/less possibility (can be/cannot be) present. In classical set theory, an element either belongs to a set or not, the same as in optimization, and a solution is therefore either feasible or not. Fuzzy set theory, coined by Zadeh (1965), involves capturing, exemplifying, and working with linguistic notions-objects for which boundaries are unclear. While the Boolean set theory (Boole, 1951) defines a membership value of either 1 or 0 (true or false), the fuzzy set theory defines the degree of membership in a set, represented by values between 0 and 1.

Typically, a fuzzy model consists of the following feed forward modules, (a) a fuzzifier (encoder: converts input categorical or numerical data into fuzzy values), (b) an inference engine (processor: the mind of the fuzzy model, simulates the human decision-making process), and (c) a defuzzifier (decoder: converts a synthesized fuzzy set back to a crisp set using a mathematical function or a subjectively or objectively defined threshold fuzzy value).

3.3.1. Fuzzifier: Fuzzification of Predictor Maps

The value of the membership function can be calculated using two methods; (a) calculate the membership function using a membership function curve, or (b) assign membership values for each class artificially based on expert knowledge of the system concerned. In this study both methods were adopted. For the factor maps of valley network (ga_vlnet), ash thickness (lk_pyash), and map of open/closed basins (tg_basin), fuzzy membership values were added manually, while the fuzzy membership values for the rest of the maps were calculated using membership function curves.

In this study, four membership functions were modeled, and results were compared to select the best method. The methods include membership function calculation using positive weight (W^+), contrast (C), and studentized contrast (C_{std}) of each map unit calculated using the WEM method.
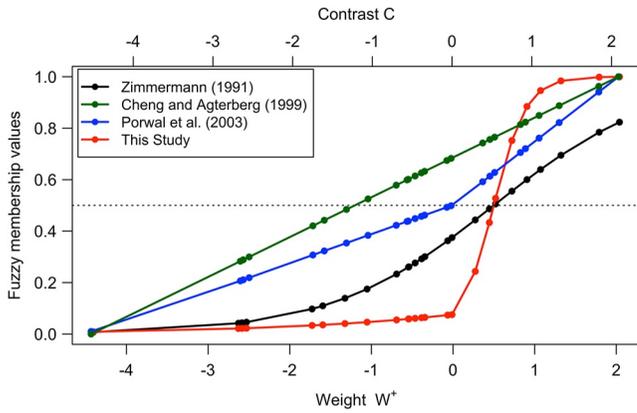
3.3.1.1. Method 1 (Zimmermann, 1991)

Logistic membership function, $\mu_A(x)$,

$$\mu_A(x) = \frac{1}{1 + e^{-a(w_{pij} - b)}} \tag{8}$$

where, w_{pij} is the positive weight of the jth class of the ith evidential map (fuzzy set), b is a specified fuzzy score at cross-over point for the function, and a is a specified slope of the function at cross-over point. Slope values, a, used for each factor map are shown in Table 2. The value of the cross-over point, b, is assigned as 0.5. The logistic membership function transforms the class weights into fuzzy membership values that range from 0 to 1.

3.3.1.2. Method 2 (Cheng & Agterberg, 1999)

Fuzzy membership values were calculated using the contrast values in each evidential map,

Figure 3. Calculation of fuzzy membership functions using different methods. The geology map (tn_geomp) was used as the example in this figure. The Weight W^+ x-axis refers to Method 1 (Zimmermann, 1991) and Method 4 developed in this study, while the Contrast C x-axis refers to Method 2 (Cheng & Agterberg, 1999) and Method 3 (Porwal et al., 2003).

$$\mu_A(x) = \frac{C_{ij} - C_{\min}}{C_{\max} - C_{\min}} \qquad (9)$$

where, $C_{\max}$ and $C_{\min}$ are the maximum contrast ($C_{\max} = \max(W^+ - W^-)$), and the minimum contrast of the ith fuzzy set, respectively. C_{ij} is the contrast value of the jth class in the ith evidential map.

3.3.1.3. Method 3 (Porwal et al., 2003)

Porwal et al. (2003) defined the piece-wise linear membership function as the fuzzifier in their model based on the contrast value. The membership value, $\mu_A(x_{ij})$ is calculated using

$$\mu_A(x) = \begin{cases} 0.01 & if\ C_{ij} = C_{min}\ \&\ C_{min} < 0 \\ 0.5 - \dfrac{C_{ij}}{2 \times C_{min}} & if\ C_{min} < C_{ij} \leq 0 \\ 0.5 + \dfrac{C_{ij}}{2 \times C_{max}} & if\ 0 \leq C_{ij} \leq C_{max} \end{cases} \qquad (10)$$

where, C_{ij} is the contrast value of the jth class of ith evidential map, and $C_{\min}$ and $C_{\max}$ are the minimum and maximum contrast values of the ith map.

3.3.1.4. Method 4 (This Study)

This study employs a Logistic membership function, $\mu_A(x)$,

$$\mu_A(x) = \frac{1}{1 + e^{-a\left((w_{pij} \times F) - b\right)}} \qquad (11)$$

where w_{pij} is the positive weight of the jth class of ith evidential map. b is a specified fuzzy score at the cross-over point for the function, a is a specified slope of the function at the cross-over point. Multiplication factor F was calculated using studentized contrast (C_{std}) of each class in each evidential map.

$$F = \begin{cases} 0.1 & C_{std} < 1.5 \\ 1.0 & C_{std} \geq 1.5 \end{cases} \qquad (12)$$

The fuzzy membership values must show not only the relative importance of each map, but also the relative importance of each class (map units) in each map. Therefore, different slope values "a" were chosen for each map based on the importance of each map and their classes (map units) (Table 2). The fuzzy membership function maps are named using the respective MapID followed by prefix fzm_.

The fuzzy membership values of the different map units in the geologic map calculated using the above four methods are shown in Figure 3. This shows that the method developed in this study (Method 4) performs the best and was therefore chosen as the fuzzy membership calculation method for this study (Table S1 in Supporting Information S1).

Figure 4 plots the fuzzy membership values against the geological map units in (relative) chronological order. It shows that high fuzzy membership values were received for the Noachian age terrains, where most hydrous mineral detections were found (Carter et al., 2013; Ehlmann & Edwards, 2014). Hesperian and Noachian highland undivided and Hesperian transition terrains (Htu and Ht) show high Fuzzy membership values after high values seen in Early and Middle Noachian highland massifs (mHnm and eNhm). The peak observed at the Late Noachian to Early-Hesperian transition has been proposed as an epoch of intense surface flow (Irwin et al., 2005). Carter et al. (2013) observed fewer hydrous mineral exposures in Hesperian aged terrain, and a negligible number of hydrous mineral exposures in Amazonian-aged terrains. Figure 4 also shows a peak for Amazonian and Hesperian impact (AHi). This might be due to the delivery of preexisting clay-rich material from underneath more recent terrains to the surface by impact excavation (Barnhart & Nimmo, 2011). It is also important to note that the number of hydrous mineral occurrences corresponding to a geologic unit does
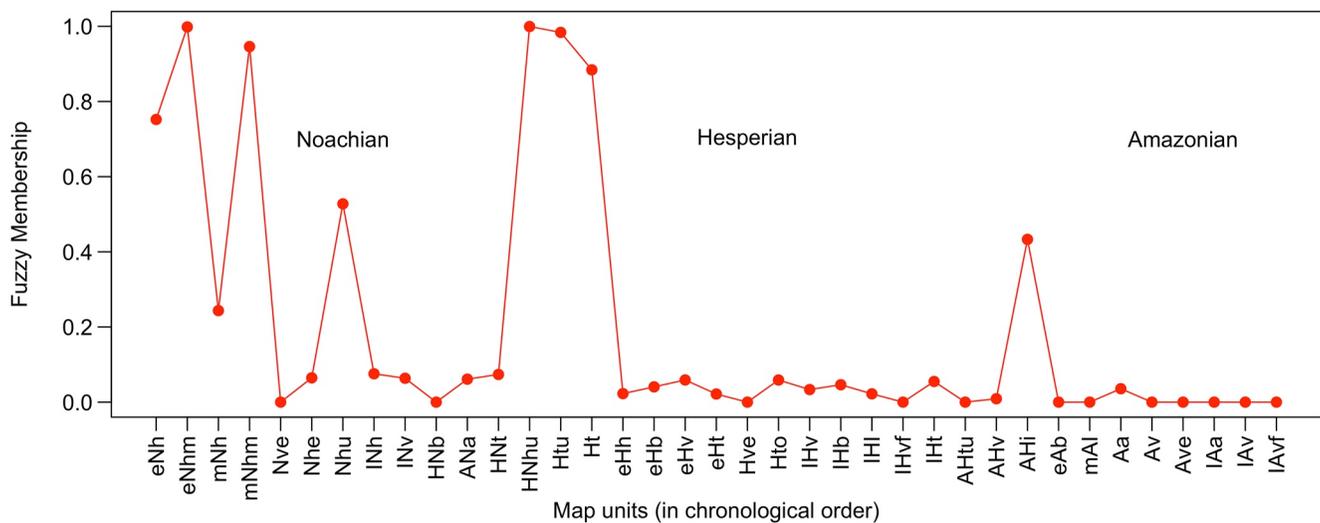
Figure 4. Calculated fuzzy membership values as a function of time (geological units). eNh, Early Noachian highland; eNhm, Early Noachian highland massif; mNh, Middle Noachian highland; mNhm, Middle Noachian highland massif; Nve, Noachian volcanic edifice; Nhe, Noachian highland edifice; Nhu, Noachian highland undivided; lNH, Late Noachian highland; lNv, Late Noachian volcanic; HNb, Hesperian and Noachian basin; ANa, Amazonian and Noachian apron; HNt, Hesperian and Noachian transition; HNhu, Hesperian and Noachian highland undivided; Htu, Hesperian transition undivided; Ht, Hesperian transition; eHh, Early Hesperian highland; eHb, Early Hesperian basin; eHv, Early Hesperian volcanic; eHt, Early Hesperian transition; Hve, Hesperian volcanic edifice; Hto, Hesperian transition outflow; lHv, Late Hesperian volcanic; lHb, Late Hesperian basin; lHl, Late Hesperian lowland; lHvf, Late Hesperian volcanic field; lHt, Lte Hesperian transition; AHtu, Amazonian and Hesperian transition undivided; AHv, Amazonian and Hesperian volcanic; AHi, Amazonian and Hesperian impact; eAb, Early Amazonian basin; mAl, Middle Amazonian lowland; Aa, Amazonian apron; Av, Amazonian volcanic; Ave, Amazonian volcanic edifice; lAa, Late Amazonian apron; lAv, Late Amazonian volcanic; lAvf, Late Amazonian volcanic field.

not necessarily reflect the time of their formation. Those hydrous mineral detections can be younger (e.g., weathering) or older (e.g., transported from other places and deposited) than the outcrop (geologic unit) in which they are present (Carter et al., 2013). The pattern of fuzzy membership values with respect to the age of Martian surface units is consistent with previous reconstructions of hydrous mineral occurrences over time (e.g., Ehlmann & Edwards, 2014), favoring the occurrence of zeolites in terrains formed during wetter intervals.

Fuzzy membership function values were manually added to the factor maps of valley network (ga_vlnet) and ash thickness (lk_pyash) (Table 3). These membership values were chosen arbitrarily based on subjective judgment about the relative importance of each class (map unit) in each factor map. As an example, based on the examples from the Earth, closer to a valley network will have higher probabilities to form zeolites and other hydrous minerals than away from the valley networks. Also, greater ash thickness will have higher probabilities to form/present zeolite minerals.
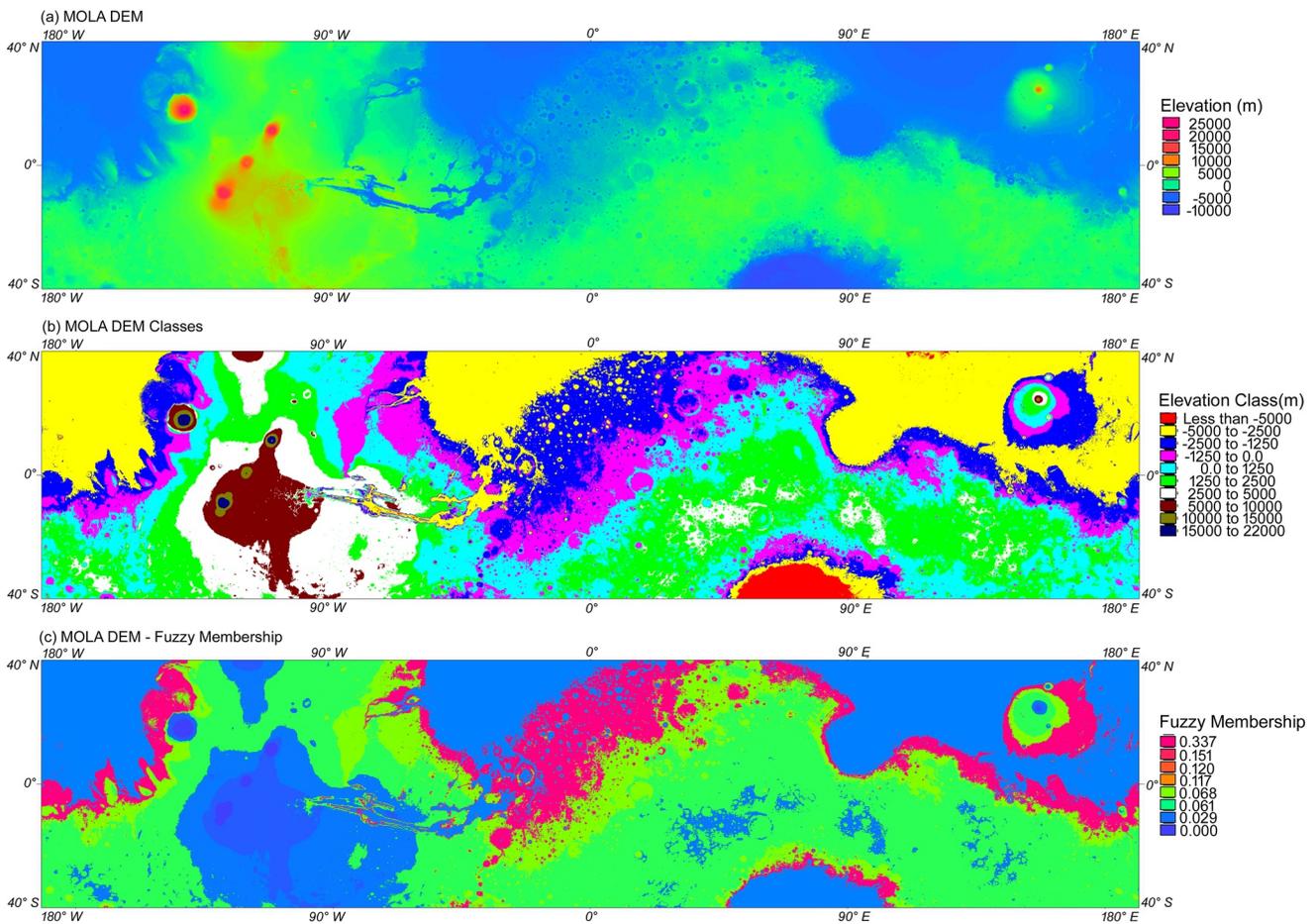
Figure 5 shows the entire fuzzification process using MOLA DEM as an example. It shows the original MOLA DEM (a), classified MOLA DEM (b) and after assigning the calculated fuzzy membership values for each elevation class (c).

3.3.2. Inference Engine

The mind of a fuzzy model, the inference engine, uses the individual fuzzy sets conveyed by the fuzzifier while filtering out the informational noise to create a synthesized fuzzy set. A fuzzy inference engine consists of multiple serial or parallel networks that use fuzzy operators to sequentially combine fuzzy sets (Porwal et al., 2003). The most basic fuzzy operators are fuzzy OR, fuzzy AND, fuzzy algebraic products, fuzzy algebraic sum (FAS), and fuzzy Gamma (γ) operator (Bonham-Carter, 1994).

Table 3

Fuzzy Membership Values (fzm) in Map Classes of Maps of Valley Networks (ga_vlnet) and Ash Thickness Map (lk_pyash)

ga_vlnet distance class	fzm_ga_vlnet	lk_pyash thickness class	fzm_lk_pyash
0–200 m	1.0	0.00–6.25 m	0.1
200–400 m	0.9	6.25–12.50 m	0.2
400–600 m	0.8	12.50–25.00 m	0.4
600–800 m	0.7	25.00–50.00 m	0.5
800–1,000 m	0.6	50.00–100.00 m	0.6
1,000–2,500 m	0.5	100.00–200.00 m	0.7
2,500–5,000 m	0.4	200.00–400.00 m	0.8
5,000–10,000 m	0.3	400.00–800.00 m	1.0
10,000–100,000 m	0.2		
>100,000 m	0.1		

Figure 5. Fuzzification process showing (a) the original Mars Orbiter Laser Altimeter (MOLA) DEM, (b) classified MOLA DEM, and (c) a map after assigning the fuzzy membership values for each elevation class.

3.3.2.1. Fuzzy OR

Fuzzy OR is similar to a Boolean OR (logical union), and the output membership values are controlled by the maximum values from any of the input maps, for any location. The fuzzy OR is defined as,

$$\mu_X = \text{MAX}(\mu_A, \mu_B, \mu_C, \dots) \tag{13}$$

where, $\mu_A m, \mu_B, \mu_C, \dots$ are membership values at a particular location (x, y) on map A, map B, map C, …, respectively. Using this operator, the combined membership value at a specific location is represented by the most suitable evidence maps. As an example, several attempts were made to derive the abundance of olivine using OMEGA and TES data, mostly due to the effect of mixing with other minerals, dust, or the effect of grain size (e.g., Brown et al., 2020). This study selected four olivine maps as factor maps and used a fuzzy OR operator to integrate those maps to extract the most suitable locations for olivine.

$$\text{e.g., max\_olivine} = \text{MAX}(\text{MAX}(\text{fzm\_om\_osp1m}, \text{fzm\_om\_osp2}, \text{fzm\_om\_osp3}), \text{zm\_ts\_olvne}) \tag{14}$$

3.3.2.2. Fuzzy AND

Fuzzy AND is similar to a Boolean AND (logical intersection) operation on classical set values of (0,1). It is defined as

$$\mu_X = \text{MIN}(\mu_A, \mu_B, \mu_C, \dots) \tag{15}$$

The effect of Fuzzy AND is to make it so the output map is controlled by the smallest fuzzy membership value at each location (Bonham-Carter, 1994). This rule is suitable for the places where two or more pieces of evidence

Table 4
Input Map Combinations Used to Create Twelve Map Combinations

Map combination	FAP_1 FAS_1	FAP_2 FAS_2	FAP_3 FAS_3	FAP_4 FAS_4	FAP_5 FAS_5	FAP_6 FAS_6
min_physical	x		x	x		
max_physical		x			x	x
min_elements			x			
max_elements	x	x				
min_minerals	x		x		x	
max_minerals		x		x		x
fzm_geology	x	x	x	x	x	x

Note. FAP, fuzzy algebraic product; FAS, fuzzy algebraic sum.

must be present together for the hypothesis to be true. In this study, as an example, selecting the minimum albedo fuzzy membership value in each corresponding pixel in albedo fuzzy membership maps derived from both OMEGA and TES data will increase the confidence of the final albedo fuzzy membership map.

$$\text{e.g., } \min\_om\_ts\_albdo = MIN(fzm\_om\_albdo, fzm\_ts\_albdo) \quad (16)$$

Finally, six maps were created combining the above fuzzy membership maps (Map combinations listed in Table 4).

$$\text{e.g., } \min\_physical = MIN(\min\_dust\_nnphs, \min\_om\_ts\_albdo, \min\_ti\_day\_ngt) \quad (17)$$

All maps created using fuzzy operators are listed in Table S2 of Supporting Information S1.

3.3.2.3. Fuzzy Algebraic Product (FAP)

The combined membership function is defined as

$$\mu_X = \prod_{i=1}^{n} \mu_i \quad (18)$$

where μ_i is the fuzzy membership function for the ith map and $i = 1, 2, 3, \ldots, n$ maps are to be combined. The combined fuzzy membership values tend to be very small with this operator, due to the effect of multiplying several numbers less than 1. The output is always smaller than, or equal to, the smallest contributing membership value (Bonham-Carter, 1994).

3.3.2.4. Fuzzy Algebraic Sum (FAS)

Fuzzy algebraic sum is complementary to the fuzzy algebraic product and defined as

$$\mu_X = 1 - \prod_{i=1}^{n} (1 - \mu_i) \quad (19)$$

The result is always larger than or equal to the largest contributing fuzzy membership value. The pieces of evidence that both favor a hypothesis reinforce one another and the combined evidence is more supportive than either piece of evidence taken individually (Bonham-Carter, 1994).

From these six map combinations created using fuzzy OR and AND operators, 12 maps were generated calculating fuzzy algebraic product (FAP) and FAS. The resulting fuzzy algebraic products (FAP) and algebraic sum (FAS) maps for the sixth map combination (FAP_6 and FAS_6 in Table 4) are shown in Figure 6.

3.3.2.5. Gamma (γ) Operation

Gamma operation is defined in terms of FAP and the FAS by

$$\mu_X = (\text{Fuzzy algebraic sum})^{\gamma} * (\text{Fuzzy algebraic product})^{1-\gamma} \quad (20)$$

where γ is a parameter chosen in the range of 0–1 (Zimmermann & Zysno, 1980). When γ is 0, the combination equals the FAP, and when the γ is 1, the combination equals the FAS. A wise selection of γ creates output values that ensure a flexible compromise between the "increasing" effects of the FAS and the "decreasing" effects of the FAP.

Twenty-five (25) maps were calculated using different map combinations listed in Table 4 with different gamma values (Table S3 in Supporting Information S1). In other words, 25 inference network models were created. After visual and statistical analysis of all 25 maps, map combinations 2 (Fz_02) and 6 (Fz_06) in Table 4 were selected for further analysis. Figure 7 shows the favorability coverage and the test and train accuracy of each map combination with respect to the gamma values. Favorability coverage was calculated based on the area with fuzzy membership values (pixel values) higher than 0.5 compared to the total map area. This shows that the percentage of (favorability) coverage and test and train accuracy of both map combinations increases with the increase of

(a) Fuzzy Algebraic Sum Map (FAS_6)

(b) Fuzzy Algebraic Product Map (FAP_6)
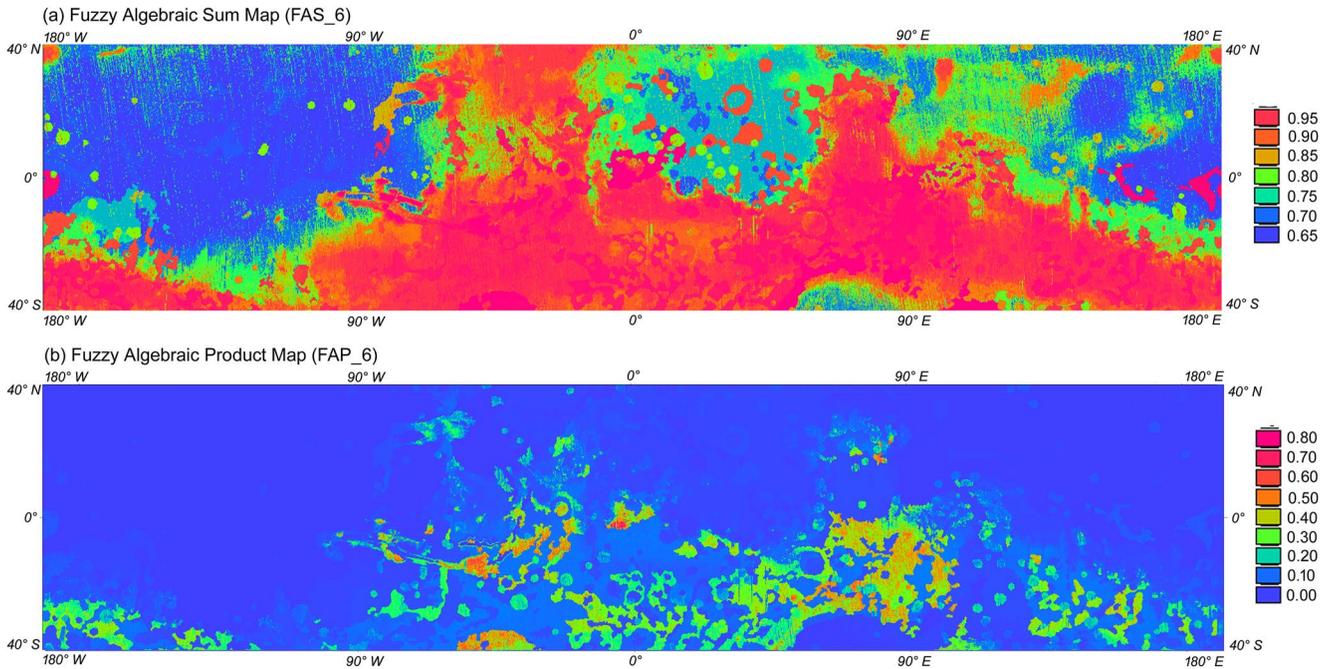
Figure 6. Fuzzy algebraic product (FAP) and fuzzy algebraic sum maps of map combination 6 (FAP_6 and FAS_6) listed in Table 4.

gamma values. The best predictive model in this case would be the model with the highest train and test accuracy and with the lowest spatial coverage. A test and train accuracy (success rate) higher than 80% was defined as the selection criterion and based on that a 0.84 gamma value was selected. However, both map combinations (F2 and F6) scored more than 80% accuracy, though the F6 shows higher spatial coverage than F2. Four favorability map classes were created from each map (Fz_02_0.84 and Fz_06_0.84, the last number after the second underscore indicates the gamma value used to create the map) based on the favorability index (pixel values). Classes include Unfavorable (pixel value 0–0.25), Less favorable (pixel value 0.25–0.50), Favorable (pixel value 0.50–0.75), and Most favorable (pixel value 0.75–1.00). This step is called defuzzification. Results were validated using train and test data sets. Table 5 shows the results of the accuracy assessment. The values are in percentages representing the number of data points in each class with respect to the total number of points in the data set. This shows that Fz_06_0.84 shows the highest test and train accuracy for the most favorable class. Therefore, map F_06_0.84 was selected as the final map to select the highest potential areas for hydrous minerals (Figure 8) and to identify the potential locations for zeolites in the next step.
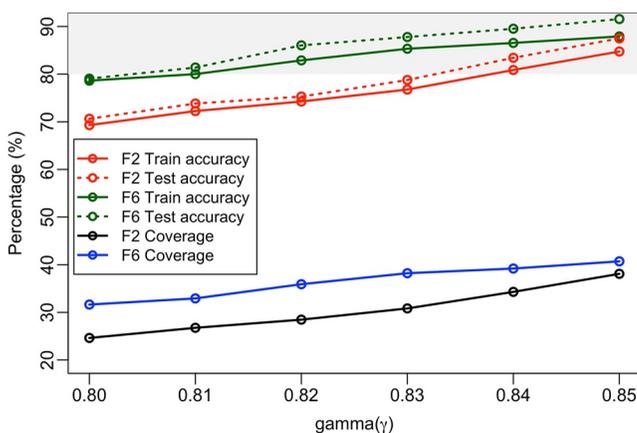
Figure 7. Percent accuracy and spatial coverage in each map combination (F2 and F6) against different gamma values.

As discussed in the introduction, the greatest abundances of zeolites on Earth are found in volcaniclastic deposits. Therefore, it is hypothesized that zeolites are most likely to be found in places where pyroclastic deposits were subjected to aqueous alteration. The possible aqueous alteration areas were mapped using hydrous mineral detections in previous steps. Ash distribution patterns on Mars modeled by Kerber et al. (2013) were used to identify the most favorable areas for zeolites on early Mars. Ash thickness in their model is proportional to the possibility that zeolites could form, because higher thickness can reflect a large amount of ash in the area or a high possibility of finding ash in the area according to the model. The map of possible pyroclastic deposits larger than 10^5 km^2 is also used in this study to achieve more robust results. The ash thickness map modeled by Kerber et al. (2013) and potential pyroclastic deposits (black outlines) are shown in Figure 9. Ash thickness in the map is represented by the fuzzy membership values. Assigned fuzzy membership values positively increase with the modeled ash thickness (Table 3).

Figure 10 shows the workflow of the three-stage inference engine used to create the final map. At the first stage, all the fuzzified evidential maps which

Table 5
*Test and Train Accuracy (Success Rate) of Each Map Combination*

Class	Fz_02_0.84_trn	Fz_02_0.84_tst	Fz_06_0.84_trn	Fz_06_0.84_tst
Unfavorable	0.1	0	0.3	0
Less favorable	18.9	16.5	13.1	10.4
Favorable	75.5	78.5	54.6	57.3
Most favorable	5.5	5.0	32.0	32.3

Note. This shows the number of hydrous mineral detections in each class as a percentage with respect to the total number of data points. The train data set is indicated by letters "_trn" after the fuzzy map Fz_02_0.84 or Fz_06_0.84, while the test data set indicated by letters "_tst."

were created using the membership functions defined by the WEM were combined using fuzzy operators to produce three intermediate fuzzy evidential maps (max_physical, max_mineral, tn_geolo). These maps were later combined using the fuzzy gamma (γ) operator to create the synthesized fuzzy favorability map for the hydrous minerals (fav_hydrous). In the third step, the hydrous mineral favorability fuzzy membership map was combined with ash thickness (lk_pyash) and pyroclastic deposits (pb_pydep) to generate a favorability map for zeolites.

4. Results and Discussion

The potential zeolite bearing terrain map calculated using the data-driven fuzzy WEM method is shown in Figure 11. This shows that the eastern and western Arabia deposits and some sites of MFF show the highest probability for finding zeolites within the previously mapped potential pyroclastic deposits. Areas of interest outside the mapped pyroclastic deposits include certain areas of Valles Marineris, Mawrth Vallis, highlands north of Hellas, and the Terra Cimmeria and Terra Sirenum regions. Since there is no ground truth yet to validate the resultant potential zeolite bearing map, we will instead consider detections of zeolite using orbital spectroscopy and the geological and hydrological settings favorable for the formation of zeolites in the area based on the literature. Favorable geological and hydrological settings for the formation of zeolites include tuff (volcanic
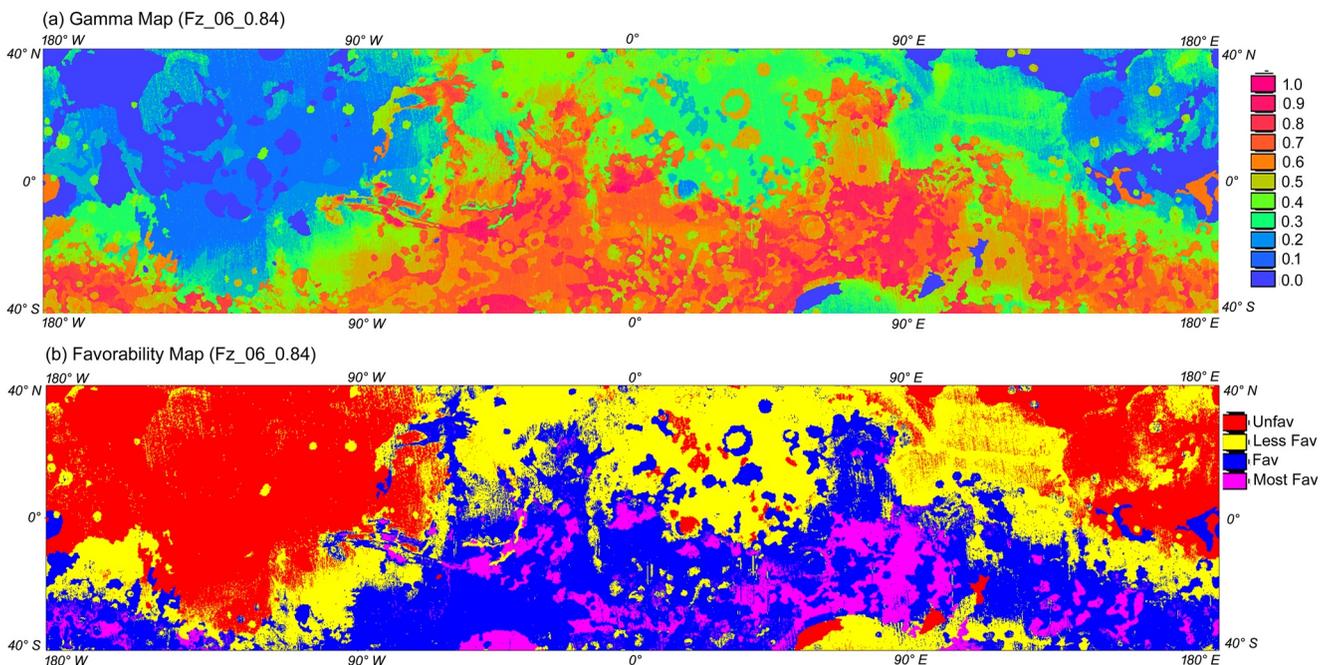

Figure 8. (a) Favorability map for hydrous minerals (Map Fz_06_0.84). The areas are ranked based on their fuzzy membership values. Fuzzy membership ranges from 0 to 1 (less favorable to highly favorable). (b) Favorability class map derived from map (a) showing the potential area for the hydrous minerals on Mars up to 40° latitude.
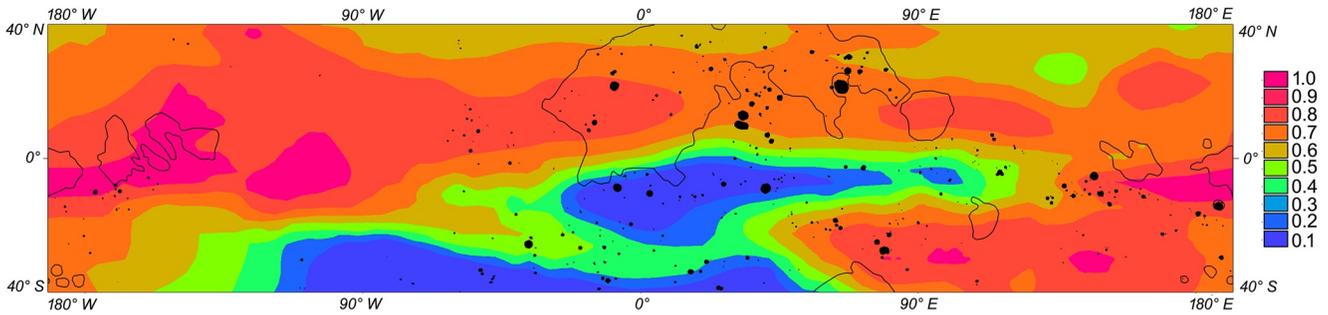
Figure 9. The map shows the thickness of possible ash deposits modeled by Kerber et al. (2013) and pyroclastic ash deposits (black outline) compiled by Broz et al. (2020). The open and closed basins compiled by Goudge et al. (2016) are also shown (black filled areas). Values in the legend are fuzzy membership values corresponding to the thickness of the modeled ash deposits.
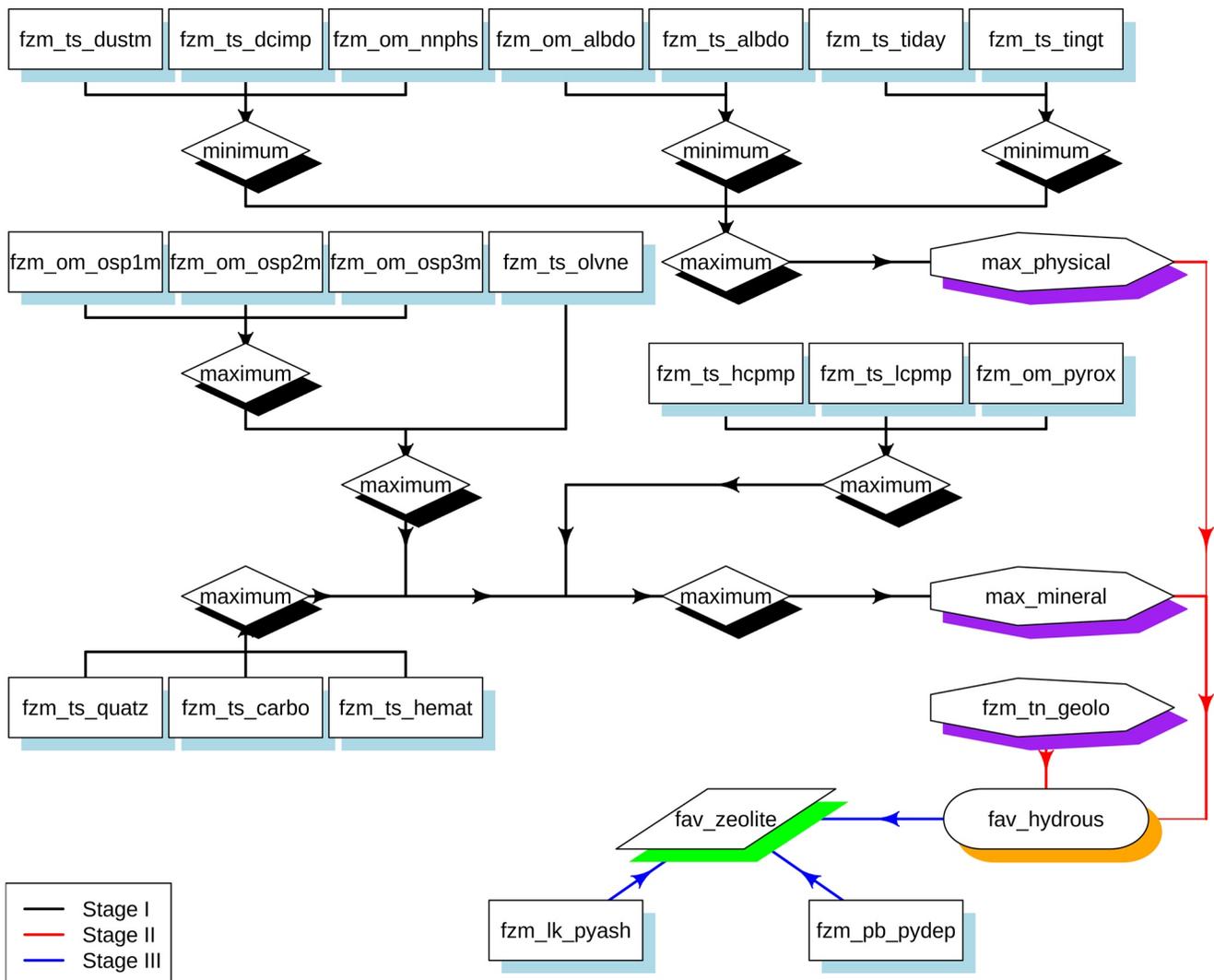
Figure 10. The fuzzy inference engine used to create the final map.
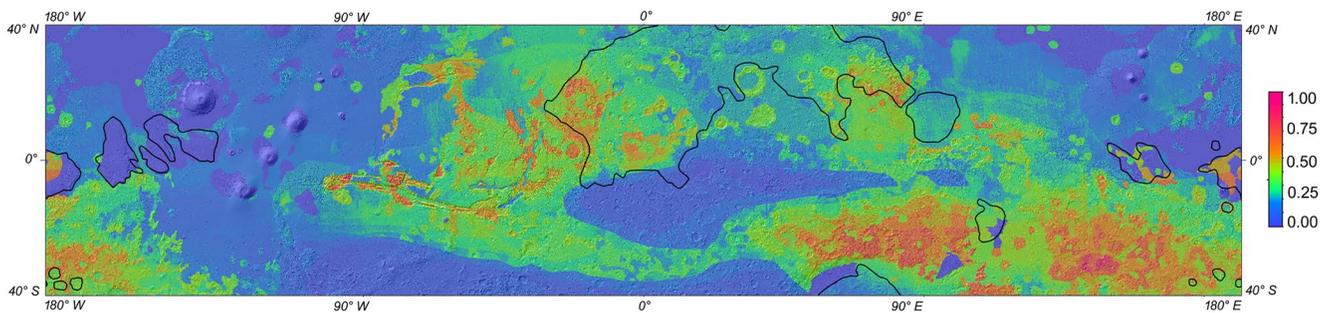
Figure 11. Potential zeolite-bearing terrains calculated using the data driven fuzzy Weights-of-Evidence method. Value range indicates the possibility of finding zeolite based on the calculations. 1 = highest possibility, 0 = Lowest possibility. Background is a hillshade from Mars Orbiter Laser Altimeter DEM.

ash deposits), water, and the presence of key hydrous minerals implying near-surface temperature alteration, low-grade metamorphic alteration, or hydrothermal alteration (e.g., Brown et al., 2010).

4.1. Potential Zeolite Bearing Terrains

4.1.1. Arabia Terra

Arabia Terra is a cratered Noachian highland area and is probably composed of a mixture of impact breccias and volcanic, aeolian, and fluvial deposits (Davis et al., 2019; Tanaka, 2000). The zeolite mineral analcime was first detected in the west of Nili Fossae in craters near the Antoniadi basin and in the eastern portion of the Arabia Terra by Ehlmann et al. (2009) using CRISM data. Ash dispersion modeling (e.g., Kerber et al., 2012, 2013) suggests that extensive ash deposits should be common in the Arabia Terra. Fassett and Head (2007) observed that hundreds of meters of material was deposited on the surface of the northeast Arabia Terra, likely as airfall. The fluvial systems in the region are interpreted to have been formed by precipitation and runoff during the mid-Noachian and early-Hesperian (Davis et al., 2016, 2019). Whelley et al. (2021) also identified the presence, thickness, and distribution of altered volcanic ash layers in Arabia Terra using orbital spectral data. They identified the inter-layered sequence of volcanic ash units containing hydroxy sulfates, Fe/Mg-smectites, Al-smectites, aluminosilicates, and hydrated silica.

4.1.2. Medusae Fossae Formation

The MFF in southern Elysium and northern Memnonia and Amazonis Planitia and Aeolis Planitia (Kerber & Head, 2010) is characterized by large accumulations of friable, fine-grained deposits most likely composed of volcanic ash, ignimbrites, or aeolian dust (Kerber & Head, 2010; Mandt et al., 2008). Both the Tharsis Montes and Elysium Montes could be the source of pyroclastic deposits. Modified and inverted fluvial channels indicate that there was some fluvial activity during the formation or modification of the MFF (Kerber & Head, 2010).

4.1.3. Valles Marineris

Viviano-Beck et al. (2017) compositionally mapped the Valles Marineris wall units and identified zeolites along with chlorite and carbonate on the north and south walls of eastern Coprates Chasma. They were spatially associated with olivine-rich dikes, suggesting hydrothermal alteration from primary igneous phases to zeolite (Viviano-Beck et al., 2017). The coexistence of zeolites and carbonates implies that the fluids were alkaline. A wide variety of hydrated mineral assemblages is also identified in a depression close to Noctis Labyrinthus, at the western end of Valles Marineris, where Figure 11 shows high probability of finding zeolites (e.g., Thollot et al., 2012). Mitrofanov et al. (2022) recently observed unusually high hydrogen abundances at Candor Chaos in the central area of Valles Marineris using the FREND (Fine Resolution Epithermal Neutron Detector) neutron telescope onboard ExoMars Trace Gas Orbiter. Based on these results, they concluded that the high (40.3%) mean derived Water Equivalent Hydrogen value at the Candor Chaos could be related to locally large abundances of highly hydrated minerals or water ice permafrost.

4.1.4. Mawrth Vallis

Mawrth Vallis sits at the boundary between the northern lowlands and the southern highlands (Bishop et al., 2013) and hosts the largest outcrop of Al/Si-rich clays on Mars (Bishop & Rampe, 2016). The Al/Si-rich clay unit

mainly consists of montmorillonite, opal, kaolinite/halloysite, aluminosilicates, and zeolite (Bishop et al., 2013). Bishop and Rampe (2016) have identified the poorly crystalline aluminosilicates as allophane and imogolite using CRISM and TES data. They suggested that the ash from one or many of the super volcanoes identified in northern Arabia Terra could be the source of allophane + imogolite unit at Mawrth Vallis. Loizeau et al. (2012) estimated the age and duration of aqueous activity in the Mawrth Vallis region using crater counting. Michalski et al. (2013) developed multiple working hypotheses as to how the compositional stratigraphy at Mawrth Vallis region formed and their favored hypothesis for the observed compositional stratigraphy was that volcanogenic acidic aerosols and snow or ice and small volumes of water chemically altered tephra deposits.

4.1.5. North Hellas Highlands

The model also shows a high favorability for zeolites in the North Hellas highland region. Terby crater in the North Hellas highlands hosts the thickest lake sediments yet observed on Mars (Ansan et al., 2011). Hargitai et al. (2018) mapped potential paleolakes to the northeast of Hellas Basin in the Navua-Hadriacus-Ausonia region, identifying 34 potentially paleolake-hosting depressions. These lakes may have formed in the Hesperian during a volcanically active period (Hargitai et al., 2018). Zhao et al. (2020) identified 64 paleolakes with diameters larger than 4 km. They observed lacustrine deposits, volcanic ash, aeolian sand deposits, exposures of bedrock, and impact breccia/melts in the area. Previous studies of the northwestern Hellas region showed high concentrations of aqueous minerals including carbonates, chlorides, sulfates, and phyllosilicates (Carter et al., 2013; Ehlmann & Edwards, 2014; Osterloo et al., 2010; Wray et al., 2016; Zhao et al., 2020).

4.1.6. Terra Cimmeria/Terra Sirenum Region

The Terra Cimmeria/Terra Sirenum region has light-toned knobs that contain phyllosilicates possibly formed by aqueous alteration of the fine-grained (potentially ashfall) Electris Deposit described by Grant and Schultz (1990). The clays in these deposits likely formed in a network of local lakes (Wendt et al., 2013). The mineralogical, morphological, and stratigraphical study of Terra Cimmeria/Terra Sirenum region by Wendt et al. (2013) shows the long-lasting, complex aqueous history involving localized lakes, valley networks, and multiple stages of mineral alteration.

4.2. Limitations and Uncertainties

The original data sets used to create factor maps have a very wide range of resolution from 18 m/pixel (CRISM target) to 300 km/pixel (GRS), due to the type of remote sensing techniques applied and the type of data acquired. This is one of the main limitations while working with different sources of data for global statistical studies since high resolution data will be averaged to a middle resolution while low resolution data will be replicated. As an example, the diversity in surface expression revealed by high resolution images such as CRISM, THEMIS and OMEGA are not detectable in the GRS low resolution images. However, CRISM, THEMIS, and OMEGA record the information on a few millimeters or the surface, while the GRS records information from the top few tens of centimeters of the surface. Therefore, it is important to keep the low-resolution data set in this case since it records different types of information that cannot be derived from the high-resolution data set. The elemental maps derived from the GRS give the opportunity to map the homogeneous elemental provinces on the surface of Mars (e.g., Gasnault et al., 2010; Karunatillake et al., 2009; Taylor et al., 2010). These elemental provinces show statistically significant similar elemental abundances representing chemically similar materials on the surface, which may be important for finding zeolites (e.g., Fialips et al., 2005). One of the main advantages of WEM is it only keeps the highly spatially correlated factor maps during the process of calculation. As an example, if the evidential map (locations of hydrous minerals) shows high spatial correlation to a certain GRS derived elemental province map, it will keep that factor map for further calculation. In this study, none of the GRS maps achieved the higher spatial correlation (positive or negative, Equations 5–7) with the evidential map and therefore did not contribute to the calculation of final map (Figure 10).

Missing data or misinterpreted patterns are two major sources of uncertainty in mapping mineral favorability. This is more critical in poorly explored areas where fewer data are available than in well-explored areas. Most areas on Mars are poorly explored. The fuzzy WEM adopted here provides a framework for calibrating fuzzy membership functions to replace missing data for posterior probability calculations (Cheng & Agterberg, 1999). Since the WEM is objective, it also avoids the subjective choice of weighting factors. The objective methods are more important in poorly explored areas where little knowledge is available. One of the main disadvantages of the WEM is that it is only applicable in regions where the response variable is fairly well known. If

the response variable is poorly known for a certain region, the results must be interpreted with caution. The response variable used in this study is the location of hydrous minerals. Carter et al. (2013) discussed several biases and limitations for hydrous mineral detections, which can directly influence the probabilistic model applied here.

1. Carter et al. (2013) demonstrated that the detection capabilities of hydrous minerals on Mars using orbital data are limited by the pixel resolution of the instrument. Areas with hydrous minerals larger than the smallest ground resolution cell (~20 m in CRISM) can be detected. In addition, orbital spectral data from both CRISM and OMEGA exhibit instrumental artifacts that can affect the identification of minerals (false positives and false negatives). Also, observational biases such as surface dust cover, ice, photometric effects, residuals in the atmospheric correction, and spectral mixing with non-hydrated minerals could affect the hydrous mineral detections from orbital data.
2. 98% of the martian surface has not yet been observed using high resolution CRISM images. Though the multi-spectral CRISM observations cover almost the entire planet, hydrous mineral detection from multispectral CRISM data is mostly discarded by Carter et al. (2013) due to their low spectral resolution.
3. Some regions have been studied more than others, resulting in more hydrous mineral detection than in the less studied areas.
4. Small hydrous mineral exposures are covered by fewer pixels and on average have spectra with lower S/N ratios, making them harder to identify.

In addition to the limitations of the response variable (hydrous mineral detection), two other types of uncertainties and errors can be mainly identified; (a) errors and uncertainties associated with the original data or introduced during the pre-processing and processing of vector/raster data and (b) errors and uncertainties introduced during the information representation and digital fusion of the factor maps (Moon, 1998). Since the global maps used in this study were of different resolutions, coordinate systems, and different file formats, errors and uncertainties can be introduced during the resampling process, reclassification process, projection and transformation, and data handling. These errors and uncertainties can transmit through the entire process and into the final results. Some of the errors and uncertainties are introduced during the information representation and digital fusion, and the methods used to eliminate some of these errors and uncertainties are briefly discussed below.

This study did not test the CI among the evidential maps, though some evidential maps seem to have a conditional dependence (e.g., Albedo, Thermal inertia, dust cover index). Conditional dependence can create problems when combining maps using fuzzy algebraic product, FAS, and γ operator. However, before applying these three operators, all the similar maps were synthesized using fuzzy OR and fuzzy AND operators to eliminate the effect of CI. Therefore, it is not necessary that conditionally dependent maps are rejected in the predictive mineral mapping process using fuzzy logic, if an appropriate inference network is used (Porwal et al., 2003). However, if extremely high or low noise values are associated with some pixels in evidential maps, it will propagate through the fuzzy OR and fuzzy AND operators to the final synthesized fuzzy favorability map (Knox-Robinson, 2000). These noise effects (no data pixels and saturated pixels) were observed in most of the used image products. If FAS and fuzzy algebraic product (FAP) operators were used individually, these noises could be amplified because of the increasing and decreasing tendencies of these two operators, respectively. The fuzzy γ operators balanced these tendencies of the FAS and FAP operators by using appropriate values of γ (Knox-Robinson, 2000; Porwal et al., 2003). One of the main advantages of fuzzy models is their capability to control the propagation of extreme-value noise to the output. Future studies will include the selection of the best sites (pixels) that have the highest favorability index for zeolites (and for which orbital spectral data are available), followed by detailed study to confirm the presence of zeolites and reconstruct their formation scenarios. In addition, the map of highly favorable areas for zeolites can also be used as a guide to search for other hydrated minerals that are formed, weathered, or altered from volcanic ash.

5. Conclusions

In this study, the data-driven fuzzy based WEM was applied to produce a hydrous mineral favorability map and a zeolite mineral favorability map of the surface of Mars up to 40° latitudes toward both poles. The results of this work lead to the following main conclusions:

1. The methods applied in this study dealt well with qualitative, quantitative, multi-resolution, multi-source data/information for Mars, acquired from orbital data, which may be imprecise and incomplete due to the limitations of spatial resolution, spatial coverage, surface dust, instrumental biases, and other intrinsic biases.
2. The WEM method provided a simple statistical method for predicting mineral potential based on limited known occurrences.
3. The most important and sensitive processes in fuzzy modeling were the definition of fuzzy membership values of multiclass evidential maps and the selection of fuzzy set operators and an appropriate inference network for combining the evidential maps.
4. The favorability map for hydrous minerals obtained by a well-tuned fuzzy inference engine indicates a strong correlation (success rate) between the areas of high favorability of hydrous minerals and known hydrous mineral detections.
5. Favorability for zeolites was derived from the favorability of hydrous mineral map and the pyroclastic deposits (modeled and confirmed) map and agrees with previous studies conducted in those favorable areas, supporting the validity of the conceptual model used and its accuracy.
6. The favorable areas for zeolites identified in this method include the eastern and western Arabia deposits and some sites in the MFF within previously mapped potential pyroclastic deposits. Favorable areas for zeolites outside the mapped pyroclastic deposits include certain areas of Valles Marineris, Mawrth Vallis, highlands north of Hellas, and the Terra Cimmeria, and Terra Sirenum regions.

Data Availability Statement

Data is available through Alemanno et al. (2018), Bandfield (2002), Boynton et al. (2004), Broz et al. (2020), Carter et al. (2013), Goudge et al. (2016), Kerber et al. (2013), Ody et al. (2012), Poulet et al. (2007), Putzig and Mellon (2007), Ruff and Christensen (2002), Smith et al. (2001), Tanaka, Robbins, et al. (2014), and Tanaka, Skinner, et al. (2014). Data analysis was done using ILWIS (ILWIS, 2005), GDAL (GDAL/ORG contributors, 2020), ISIS3 (Adoram-Kershner et al., 2020), R (R Core Team, 2021), and RStudio (RStudio Team, 2020) software packages. Figures were made using ILWIS (ILWIS, 2005) and the R statistical software package (R Core Team, 2021).

References

Adoram-Kershner, L., Berry, K., Lee, K., Laura, J., Mapel, J., Paquette, A., et al. (2020). USGS-Astrogeology/ISIS3: ISIS3.10.1 Public Release (3.10.1) [Data]. Zenodo. https://doi.org/10.5281/zenodo.3697255

Alemanno, G., Orofino, V., & Mancarella, F. (2018). Global map of Martian fluvial systems: Age and total eroded volume estimations. *Earth and Space Science*, *5*(10), 560–677. https://doi.org/10.1029/2018ea000362

Ansan, V., Loizeau, D., Mangold, N., Le Mouélic, S., Carter, J., Poulet, F., et al. (2011). Stratigraphy, mineralogy, and origin of layered deposits inside Terby Crater, Mars. *Icarus*, *211*(1), 273–304. https://doi.org/10.1016/j.icarus.2010.09.011

Bandfield, J. L. (2002). Global mineral distributions on Mars. *Journal of Geophysical Research*, *107*(E6), 5042. https://doi.org/10.1029/2001JE001510

Bandfield, J. L., Glotch, T. D., & Christensen, P. R. (2003). Spectroscopic identification of carbonate minerals in the Martian dust. *Science*, *301*(5636), 1084–1087. https://doi.org/10.1126/science.1088054

Barnhart, C. J., & Nimmo, F. (2011). Role of impact excavation in distributing clays over Noachian surfaces. *Journal of Geophysical Research*, *116*(E1), E01009. https://doi.org/10.1029/2010je003629

Basu, A., Schmitt, J., & Crossey, L. J. (1998). An argument for zeolites in Mars rocks and an Earth analog. In *Proceedings of the Lunar Planet Science Conference 24th Abstract* (Vol. 1041).

Berkley, J. L., & Drake, M. J. (1981). Weathering of Mars: Antarctic analog studies. *Icarus*, *45*(1), 231–249. https://doi.org/10.1016/0019-1035(81)90016-6

Bish, D. L., Carey, J. W., Vaniman, D. T., & Chipera, S. J. (2003). Stability of hydrous minerals on the martian surface. *Icarus*, *164*(1), 96–103. https://doi.org/10.1016/s0019-1035(03)00140-4

Bishop, J. L., Loizeau, D., McKeown, N. K., Saper, L., Dyar, M. D., Des Marais, D. J., et al. (2013). What the ancient phyllosilicates at Mawrth Vallis can tell us about possible habitability on early Mars. *Planetary and Space Science*, *86*, 130–149. https://doi.org/10.1016/j.pss.2013.05.006

Bishop, J. L., & Rampe, E. B. (2016). Evidence for a changing Martian climate from the mineralogy at Mawrth Vallis. *Earth and Planetary Science Letters*, *448*, 42–48. https://doi.org/10.1016/j.epsl.2016.04.031

Boatwright, B. D., & Head, J. W. (2021). A Noachian proglacial paleolake on Mars: Fluvial activity and lake formation within a closed-source drainage basin crater and implications for early Mars climate. *The Planetary Science Journal*, *2*, 52. https://doi.org/10.3847/psj/abe773

Boatwright, B. D., & Head, J. W. (2022). Noachian proglacial paleolakes on Mars: Regionally recurrent fluvial activity and lake formation within closed-source drainage basin craters. *The Planetary Science Journal*, *3*(2), 38. https://doi.org/10.3847/psj/ac4d36

Bonham-Carter, G. F. (1994). *Geographic Information Systems for Geoscientists: Modelling with GIS*. Pergamon.

Bonham-Carter, G. F., Agterberg, F. P., & Wright, D. F. (1989). Weights of evidence modelling: A new approach to mapping mineral potential. In F. P. Agterberg & G. F. Bonham-Carter (Eds.), *Statistical Applications in the Earth Sciences* (pp. 171–183). Geological Survey of Canada.

Boole, G. (1951). *An investigation of the laws of thought* (p. 424). Dover Publications.

Boynton, W. V., Feldman, W. C., Mitrofanov, I. G., Evans, L. G., Reedy, R. C., Squyres, S. W., et al. (2004). The Mars Odyssey Gamma-ray spectrometer instrument suite. *Space Science Reviews*, *110*(1/2), 37–83. https://doi.org/10.1023/b:spac.0000021007.76126.15

Boynton, W. V., Taylor, G. J., Evans, L. G., Reedy, R. C., Starr, R., Janes, D. M., et al. (2007). Concentration of H, Si, Cl, K, Fe, and Th in the low- and mid-latitude regions of Mars. *Journal of Geophysical Research*, *112*(E12), E12S99. https://doi.org/10.1029/2007JE002887

Brown, A. J., Hook, S. J., Baldridge, A. M., Crowley, J. K., Bridges, N. T., Thomson, B. J., et al. (2010). Hydrothermal formation of clay-carbonate alteration assemblages in the Nili Fossae region of Mars. *Earth and Planetary Science Letters*, *297*(1–2), 174–182. https://doi.org/10.1016/j.epsl.2010.06.018

Brown, A. J., Viviano, C. E., & Goudge, T. A. (2020). Olivine-carbonate mineralogy of the Jezero crater region. *Journal of Geophysical Research: Planets*, *125*(3), e2019JE006011. https://doi.org/10.1029/2019JE006011

Broz, P., Bernhardt, H., Conway, S. J., & Parekh, R. (2020). An overview of explosive volcanism on Mars. *Journal of Volcanology and Geothermal Research*, *409*, 107125. https://doi.org/10.1016/j.jvolgeores.2020.107125

Cabrol, N. A., & Grin, E. A. (1999). Distribution, classification, and ages of martian impact crater lakes. *Icarus*, *142*(1), 160–172. https://doi.org/10.1006/icar.1999.6191

Cannon, K. M., Mustard, J. F., & Salvatore, M. R. (2015). Alteration of immature sedimentary rocks on Earth and Mars: Recording aqueous and surface–atmosphere processes. *Earth and Planetary Science Letters*, *417*, 78–86. https://doi.org/10.1016/j.epsl.2015.02.017

Carr, M. H., & Chuang, F. C. (1997). Martian drainage densities. *Journal of Geophysical Research*, *102*(E4), 9145–9152. https://doi.org/10.1029/97je00113

Carranza, E. J. M. (2011). Geocomputation of mineral exploration targets. *Computers & Geosciences*, *37*(12), 1907–1916. https://doi.org/10.1016/j.cageo.2011.11.009

Carter, J., Poulet, F., Bibring, J.-P., Mangold, N., & Murchie, S. (2013). Hydrous minerals on Mars as seen by the CRISM and OMEGA imaging spectrometers: Updated global view. *Journal of Geophysical Research: Planets*, *118*(4), 831–858. https://doi.org/10.1029/2012je004145

Cheng, Q., & Agterberg, F. P. (1999). Fuzzy Weights of Evidence method and its application in mineral potential mapping. *Natural Resources Research*, *8*(1), 27–35. https://doi.org/10.1023/a:1021677510649

Chipera, S. J., & Apps, J. A. (2001). Geochemical stability of natural zeolites. *Reviews in Mineralogy & Geochemistry*, *45*(1), 117–161. https://doi.org/10.2138/rmg.2001.45.3

Christensen, P. R., Anderson, D. L., Chase, S. C., Clark, R. N., Kieffer, H. H., Malin, M. C., et al. (1992). Thermal emission spectrometer experiment: Mars Observer Mission. *Journal of Geophysical Research*, *97*(E5), 7719–7724. https://doi.org/10.1029/92je00453

Christensen, P. R., Bandfield, J. L., Hamilton, V. E., Ruff, S. W., Kieffer, H. H., Titus, T. N., et al. (2001). Mars Global Surveyor Thermal Emission Spectrometer experiment: Investigation description and surface science results. *Journal of Geophysical Research*, *106*(E10), 23823–23871. https://doi.org/10.1029/2000je001370

Davis, J. M., Balme, M., Grindrod, P. M., Williams, R. M. E., & Gupta, S. (2016). Extensive Noachian fluvial systems in Arabia Terra: Implications for early Martian climate. *Geology*, *44*(10), 847–850. https://doi.org/10.1130/g38247.1

Davis, J. M., Gupta, S., Balme, M., Grindrod, P. M., Fawdon, P., Dickeson, Z. D., & Williams, R. M. E. (2019). A diverse array of fluvial depositional systems in Arabia Terra: Evidence for mid-Noachian to early Hesperian rivers on Mars. *Journal of Geophysical Research: Planets*, *124*(7), 1913–1934. https://doi.org/10.1029/2019je005976

Dibble, W. E., & Tiller, W. A. (1981). Kinetic model of zeolite paragenesis in tuffaceous sediments. *Clays and Clay Minerals*, *29*(5), 323–330. https://doi.org/10.1346/ccmn.1981.0290502

Dickinson, W. W., & Rosen, M. R. (2003). Antarctic permafrost: An analogue for water and diagenetic minerals on Mars. *Geology*, *31*(3), 199–202. https://doi.org/10.1130/0091-7613(2003)031<0199:apaafw>2.0.co;2

Ehlmann, B. L., & Edwards, C. S. (2014). Mineralogy of the Martian surface. *Annual Review of Earth and Planetary Sciences*, *42*(1), 291–315. https://doi.org/10.1146/annurev-earth-060313-055024

Ehlmann, B. L., Mustard, J. F., Swayze, G. A., Clark, R. N., Bishop, J. L., Poulet, F., et al. (2009). Identification of hydrated silicate minerals on Mars using MRO-CRISM: Geologic context near Nili Fossae and implications for aqueous alteration. *Journal of Geophysical Research*, *114*(E2), E00D08. https://doi.org/10.1029/2009JE003339

Fassett, C. I., & Head, J. W. (2007). Layered mantling deposits in Northeast Arabia Terra, Mars: Noachian-Hesperian sedimentation, erosion, and terrain inversion. *Journal of Geophysical Research*, *112*(E8), E08002. https://doi.org/10.1029/2006je002875

Fassett, C. I., & Head, J. W. (2008). Valley network-fed, open-basin lakes on Mars: Distribution and implications for Noachian surface and subsurface hydrology. *Icarus*, *198*(1), 37–56. https://doi.org/10.1016/j.icarus.2008.06.016

Fialips, C. I., Carey, J. W., Vaniman, D. T., Bish, D. L., Feldman, W. C., & Mellon, M. T. (2005). Hydration state of zeolites, clays, and hydrated salts under present-day martian surface conditions: Can hydrous minerals account for Mars Odyssey observations of near-equatorial water-equivalent hydrogen? *Icarus*, *178*(1), 74–83. https://doi.org/10.1016/j.icarus.2005.04.020

Gasnault, O., Taylor, G. J., Karunatillake, S., Dohm, J., Newsom, H., Forni, O., et al. (2010). Quantitative geochemical mapping of Martian elemental provinces. *Icarus*, *207*(1), 226–247. https://doi.org/10.1016/j.icarus.2009.11.010

GDAL/OGR contributors. (2020). GDAL/OGR geospatial data abstraction software library. Retrieved from https://gdal.org

Goudge, T. A., Aureli, K. L., Head, J. W., Fassett, C. I., & Mustard, J. F. (2015). Classification and analysis of candidate impact crater-hosted closed-basin lakes on Mars. *Icarus*, *260*, 346–367. https://doi.org/10.1016/j.icarus.2015.07.026

Goudge, T. A., Fassett, C. I., Head, J. W., Mustard, J. F., & Aureli, K. L. (2016). Insights into surface runoff on early Mars from paleolake basin morphology and stratigraphy. *Geology*, *44*(6), 419–422. https://doi.org/10.1130/G37734.1

Goudge, T. A., Head, J. W., Mustard, J. F., & Fassett, C. I. (2012). An analysis of open-basin lake deposits on Mars: Evidence for the nature of associated lacustrine deposits and post-lacustrine modification processes. *Icarus*, *219*(1), 211–229. https://doi.org/10.1016/j.icarus.2012.02.027

Grant, J. A., & Schultz, P. H. (1990). Gradational epochs on Mars: Evidence from west-northwest of Isidis Basin and Electris. *Icarus*, *84*(1), 166–195. https://doi.org/10.1016/0019-1035(90)90164-5

Hargitai, H. I., Gulick, V. C., & Glines, N. H. (2018). Paleolakes of northeast Hellas: Precipitation, groundwater-fed, and fluvial lakes in the Navua–Hadriacus–Ausonia region, Mars. *Astrobiology*, *18*(11), 1435–1459. https://doi.org/10.1089/ast.2018.1816

Hay, R. L. (1966). Zeolites and zeolitic reactions in sedimentary rocks, *Special GSA Papers* (Vol. 85, p. 130).

Hay, R. L., & Sheppard, R. A. (2001). Occurrence of zeolites in sedimentary rocks: An overview. In D. L. Bish & D. Ming (Eds.), *Natural Zeolites: Occurrence, Properties, Applications*, *Reviews in Mineralogy and Geochemistry* (Vol. 45, pp. 217–234).

Hynek, B. M., Beach, M., & Hoke, M. R. T. (2010). Updated global map of Martian valley networks and implications for climate and hydrologic processes. *Journal of Geophysical Research*, *115*(E9), E09008. https://doi.org/10.1029/2009JE003548

Iijima, A. (1988). Chapter 3. Diagenetic transformations of minerals as exemplified by zeolites and silica minerals - A Japanese view. In G. V. Chilingarian & K. H. Wolf (Eds.), *Developments in Sedimentology*, *Diagenesis II* (Vol. 43, pp. 147–211).

ILWIS. (2005). *Integrated Land and Water Information System, Version 3.3*. Academic, ITC. Retrieved from https://www.itc.nl/ilwis/

Irwin, R. P., Howard, A. D., Craddock, R. A., & Moore, J. M. (2005). An intense terminal epoch of widespread fluvial activity on early Mars: 2. Increased runoff and paleolake development. *Journal of Geophysical Research*, *110*(E12), E12S15. https://doi.org/10.1029/2005je002460

Karunatillake, S., Wray, J. J., Squyres, S. W., Taylor, G. J., Gasnault, O., McLennan, S. M., et al. (2009). Chemically striking regions on Mars and Stealth revisited. *Journal of Geophysical Research*, *114*(E12), E12001. https://doi.org/10.1029/2008JE003303

Kerber, L., Forget, F., Madeleine, J.-B., Wordsworth, R., Head, J. W., & Wilson, L. (2013). The effect of atmospheric pressure on the dispersal of pyroclasts from martian volcanoes. *Icarus*, *223*(1), 149–156. https://doi.org/10.1016/j.icarus.2012.11.037

Kerber, L., & Head, J. W. (2010). The age of the Medusae Fossae Formation: Evidence of Hesperian emplacement from crater morphology, stratigraphy, and ancient lava contacts. *Icarus*, *206*(2), 669–684. https://doi.org/10.1016/j.icarus.2009.10.001

Kerber, L., Head, J. W., Madeleine, J.-B., Forget, F., & Wilson, L. (2012). The dispersal of pyroclasts from ancient explosive volcanoes on Mars: Implications for the friable layered deposits. *Icarus*, *219*(1), 358–381. https://doi.org/10.1016/j.icarus.2012.03.016

Knox-Robinson, C. M. (2000). Vectorial Fuzzy Logic: A novel technique for enhanced mineral perspectivity mapping, with reference to the orogenic gold mineralization potential of the Kalgoorlie Terrane, Western Australia. *Australian Journal of Earth Sciences*, *47*(5), 929–941. https://doi.org/10.1046/j.1440-0952.2000.00816.x

Kodikara, G. R. L., & McHenry, L. (2021). Self-Organizing Maps for identification of zeolitic diagenesis patterns in closed hydrologic systems on the Earth and its implications for Mars. *International Journal of Sediment Research*, *36*(5), 567–576. https://doi.org/10.1016/j.ijsrc.2021.04.003

Kodikara, G. R. L., McHenry, L. J., & Grundl, T. J. (2023). Possible formation pathways for zeolites in closed-basin lakes on Noachian Mars: Insights from geochemical modeling. *Icarus*, *389*, 115271. https://doi.org/10.1016/j.icarus.2022.115271

Kodikara, G. R. L., McHenry, L. J., & van der Meer, F. D. (2022). Application of deep learning and spectral deconvolution for estimating mineral abundances of zeolite, Mg-sulfate and montmorillonite mixtures and its implications for Mars. *Planetary and Space Science*, *223*, 105579. https://doi.org/10.1016/j.pss.2022.105579

Kodikara, G. R. L., McHenry, L. J., & van der Meer, F. D. (2023). Spectral mapping of zeolite bearing paleolake deposits at Lake Tecopa, California and its implications for mapping zeolites on Mars. *Geosystems and Geoenvironment*, *2*(1), 100119. https://doi.org/10.1016/j.geogeo.2022.100119

Lander, R. H., & Hay, R. L. (1993). Hydrogeologic control on zeolitic diagenesis of the White River sequence. *Geological Society of America Bulletin*, *105*(3), 361–376. https://doi.org/10.1130/0016-7606(1993)105<0361:hcozdo>2.3.co;2

Lee, Y. I. (1988). Chemistry and origin of zeolites in sandstones at DSDP Sites 445 and 446, Daito Ridge and Basin Province, Northwest Pacific. *Chemical Geology*, *67*(3–4), 261–273. https://doi.org/10.1016/0009-2541(88)90132-5

Loizeau, D., Werner, S. C., Mangold, N., Bibring, J.-P., & Vago, J. L. (2012). Chronology of deposition and alteration in the Mawrth Vallis region, Mars. *Planetary and Space Science*, *72*(1), 31–43. https://doi.org/10.1016/j.pss.2012.06.023

Luo, W., & Stepinski, T. F. (2009). Computer-generated global map of valley networks on Mars. *Journal of Geophysical Research*, *114*(E11), E11010. https://doi.org/10.1029/2009je003357

Luo, X., & Dimitrakopoulos, R. (2003). Data-driven fuzzy analysis in quantitative mineral resource assessment. *Computers & Geosciences*, *29*(1), 3–13. https://doi.org/10.1016/s0098-3004(02)00078-x

Mandt, K. E., de Silva, S. L., Zimbelman, J. R., & Crown, D. A. (2008). Origin of the Medusae Fossae Formation, Mars: Insights from a synoptic approach. *Journal of Geophysical Research*, *113*(E12), E12011. https://doi.org/10.1029/2008je003076

McHenry, L. J., Kodikara, G. R. L., Stanistreet, I. G., Stollhofen, H., Njau, J. K., Schick, K., & Toth, N. (2020). Lake conditions and detrital sources of Paleolake Olduvai, Tanzania, reconstructed using X-ray diffraction analysis of cores. *Palaeogeography, Palaeoclimatology, Palaeoecology*, *556*, 109855. https://doi.org/10.1016/j.palaeo.2020.109855

Mellon, M. T., Jakosky, B. M., & Kieffer, H. H. (2000). High-resolution thermal inertia mapping from the Mars Global Surveyor Thermal Emission Spectrometer. *Icarus*, *148*(2), 437–455. https://doi.org/10.1006/icar.2000.6503

Michalski, J. R., Niles, P. B., Cuadros, J., & Baldridge, A. M. (2013). Multiple working hypotheses for the formation of compositional stratigraphy on Mars: Insights from the Mawrth Vallis region. *Icarus*, *226*(1), 816–840. https://doi.org/10.1016/j.icarus.2013.05.024

Ming, D. W., & Gooding, J. L. (1988). Zeolites on Mars: Possible environmental indicators in soils and sediments. In *Workshop on Mars Sample Return Science, LPI Technical Report 88-07* (pp. 124–125). Lunar & Planetary Institute.

Mitrofanov, I., Malakhov, A., Djachkova, M., Golovin, D., Litvak, M., Mokrousov, M., et al. (2022). The evidence for unusually high hydrogen abundances in the central part of Valles Marineris on Mars. *Icarus*, *374*, 114805. https://doi.org/10.1016/j.icarus.2021.114805

Moon, W. M. (1998). Integration and fusion of geological exploration data: A theoretical review of fuzzy logic approach. *Geoscience Journal*, *2*(4), 175–183. https://doi.org/10.1007/bf02910163

Neuhäuser, B., & Terhorst, B. (2007). Landslide susceptibility assessment using "Weights-of-Evidence" applied to a study area at the Jurassic escarpment (SW-Germany). *Geomorphology*, *86*(1–2), 12–24. https://doi.org/10.1016/j.geomorph.2006.08.002

Ody, A., Poulet, F., Langevin, Y., Bibring, J.-P., Bellucci, G., Altieri, F., et al. (2012). Global maps of anhydrous minerals at the surface of Mars from OMEGA/MEx. *Journal of Geophysical Research*, *117*(E11), E00J14. https://doi.org/10.1029/2012JE004117

Ojha, L., Karunatillake, S., Karimi, S., & Buffo, J. (2021). Amagmatic hydrothermal systems on Mars from radiogenic heat. *Nature Communications*, *12*(1), 1754. https://doi.org/10.1038/s41467-021-21762-8

Osterloo, M. M., Anderson, F. S., Hamilton, V. E., & Hynek, B. M. (2010). Geologic context of proposed chloride-bearing materials on Mars. *Journal of Geophysical Research*, *115*(E10), E10012. https://doi.org/10.1029/2010JE003613

Pan, G., & Harris, D. P. (2000). *Information synthesis for mineral exploration*. Oxford University Press.

Pleskot, L. K., & Miner, E. D. (1981). Time variability of Martian bolometric albedo. *Icarus*, *45*(1), 179–201. https://doi.org/10.1016/0019-1035(81)90013-0

Porwal, A., Carranza, E. J. M., & Hale, M. (2003). Knowledge-driven and data-driven fuzzy models for predictive mineral potential mapping. *Natural Resources Research*, *12*(1), 1–25. https://doi.org/10.1023/a:1022693220894

Poulet, F., Gomez, C., Bibring, J.-P., Langevin, Y., Gondet, B., Pinet, P., et al. (2007). Martian surface mineralogy from Observatoire Pour La Minéralogie, l'Eau, les Glaces et l'Activité on board the Mars Express Spacecraft (OMEGA/MEx): Global mineral maps. *Journal of Geophysical Research*, *112*(E8), E08S02. https://doi.org/10.1029/2006JE002840

Putzig, N. E., & Mellon, M. T. (2007). Apparent thermal inertia and the surface heterogeneity of Mars. *Icarus*, *191*(1), 68–94. https://doi.org/10.1016/j.icarus.2007.05.013

Ramirez, R. M. (2017). A warmer and wetter solution for early Mars and the challenges with transient warming. *Icarus*, *297*, 71–82. https://doi.org/10.1016/j.icarus.2017.06.025

R Core Team. (2021). *R: A language and environment for statistical computing*. R Foundation for Statistical Computing. Retrieved from https://www.R-project.org/

Renaut, R. W. (1993). Zeolitic diagenesis of late Quaternary fluviolacustrine sediments and associated calcrete formation in the Lake Bogoria Basin, Kenya Rift Valley. *Sedimentology*, *40*(2), 271–301. https://doi.org/10.1111/j.1365-3091.1993.tb01764.x

Romero-Calcerrada, R., & Luque, S. (2006). Habitat quality assessment using Weights-of-Evidence based GIS modelling: The case of Picoides Tridactylus as species indicator of the biodiversity value of the Finnish forest. *Ecological Modelling*, *196*(1–2), 62–76. https://doi.org/10.1016/j.ecolmodel.2006.02.017

RStudio Team. (2020). *RStudio: Integrated Development for R. RStudio*. PBC. Retrieved from http://www.rstudio.com/

Ruff, S. W. (2004). Spectral evidence for zeolite in the dust on Mars. *Icarus*, *168*(1), 131–143. https://doi.org/10.1016/j.icarus.2003.11.003

Ruff, S. W., & Christensen, P. R. (2002). Bright and dark regions on Mars: Particle size and mineralogical characteristics based on thermal emission spectrometer data. *Journal of Geophysical Research*, *107*(E12), 2-1–2-22. https://doi.org/10.1029/2001JE001580

Schumm, S. A. (1991). *To interpret the Earth: Ten ways to be wrong*. Cambridge University Press.

Semprich, J., Schwenzer, S. P., Treiman, A. H., & Filiberto, J. (2019). Phase equilibria modeling of low-grade metamorphic Martian rocks. *Journal of Geophysical Research: Planets*, *124*(3), 681–702. https://doi.org/10.1029/2018je005869

Sheppard, R. A., & Gude, A. J. (1968). *Distribution and genesis of authigenic silicate minerals in tuffs of Pleistocene Lake Tecopa, Inyo County California*, *Geological Survey Professional Paper* (Vol. 597, p. 38). United States Government Printing Office.

Sheppard, R. A., Gude, A. J., & Fitzpatrick, J. J. (1988). Distribution, characterization, and genesis of mordenite in Miocene silicic tuffs at Yucca Mountain, Nye County, Nevada. *U. S. Geological Survey Bulletin*, *1777*, 27.

Sheppard, R. A., & Hay, R. L. (2001). Formation of zeolites in open hydrologic systems. In D. L. Bish & D. Ming (Eds.), *Natural Zeolites: Occurrence, Properties, Applications. Reviews in Mineralogy and Geochemistry* (pp. 261–275).

Smith, D. E., Zuber, M. T., Frey, H. V., Garvin, J. B., Head, J. W., Muhleman, D. O., et al. (2001). Mars Orbiter Laser Altimeter: Experiment summary after the first year of global mapping of Mars. *Journal of Geophysical Research*, *106*(E10), 23689–23722. https://doi.org/10.1029/2000je001364

Sun, V. Z., & Milliken, R. E. (2015). Ancient and recent clay formation on Mars as revealed from a global survey of hydrous minerals in crater central peaks. *Journal of Geophysical Research: Planets*, *120*(12), 2293–2332. https://doi.org/10.1002/2015je004918

Tanaka, K. L. (2000). Dust and ice deposition in the Martian geologic record. *Icarus*, *144*(2), 254–266. https://doi.org/10.1006/icar.1999.6297

Tanaka, K. L., Robbins, S. J., Fortezzo, C. M., Skinner, J. A., & Hare, T. M. (2014). The digital global geologic map of Mars: Chronostratigraphic ages topographic and crater morphologic characteristics, and updated resurfacing history. *Planetary and Space Science*, *95*, 11–24. https://doi.org/10.1016/j.pss.2013.03.006

Tanaka, K. L., Skinner, J. A., Dohm, J. M., Irwin, R. P., Kolb, E. J., Fortezzo, C. M., et al. (2014). Geologic map of Mars, *U.S. Geological Survey Scientific Investigations Map 3292, Scale 1:20,000,000, Pamphlet* (p. 43).

Taylor, G. J., Martel, L. M. V., Karunatillake, S., Gasnault, O., & Boynton, W. V. (2010). Mapping Mars geochemically. *Geology*, *38*(2), 183–186. https://doi.org/10.1130/g30470.1

Thollot, P., Mangold, N., Ansan, V., Mouélic, S. L., Milliken, R. E., Bishop, J. L., et al. (2012). Most Mars minerals in a nutshell: Various alteration phases formed in a single environment in Noctis Labyrinthus. *Journal of Geophysical Research*, *117*(E11), E00J06. https://doi.org/10.1029/2011JE004028

Tokano, T., & Bish, D. L. (2005). Hydration state and abundance of zeolites on Mars and the water cycle. *Journal of Geophysical Research*, *110*(E12), E12S08. https://doi.org/10.1029/2005JE002410

Viviano-Beck, C. E., Murchie, S. L., Beck, A. W., & Dohm, J. M. (2017). Compositional and structural constraints on the geologic history of eastern Tharsis Rise, Mars. *Icarus*, *284*, 43–58. https://doi.org/10.1016/j.icarus.2016.09.005

Wendt, L., Bishop, J. L., & Neukum, G. (2013). Knob fields in the Terra Cimmeria/Terra Sirenum region of Mars: Stratigraphy, mineralogy and morphology. *Icarus*, *225*(1), 200–215. https://doi.org/10.1016/j.icarus.2013.03.020

Whelley, P., Novak, A. M., Richardson, J., Bleacher, J., Mach, K., & Smith, R. N. (2021). Stratigraphic evidence for early martian explosive volcanism in Arabia Terra. *Geophysical Research Letters*, *48*(15), e2021GL094109. https://doi.org/10.1029/2021gl094109

Wilson, L., & Head, J. W. (2007). Explosive volcanic eruptions on Mars: Tephra and accretionary lapilli formation, dispersal and recognition in the geologic record. *Journal of Volcanology and Geothermal Research*, *163*(1–4), 83–97. https://doi.org/10.1016/j.jvolgeores.2007.03.007

Wray, J. J., Milliken, R. E., Dundas, C. M., Swayze, G. A., Andrews-Hanna, J. C., Baldridge, A. M., et al. (2011). Columbus crater and other possible groundwater-fed paleolakes of Terra Sirenum, Mars. *Journal of Geophysical Research*, *116*(E1), 41. https://doi.org/10.1029/2010je003694

Wray, J. J., Murchie, S. L., Bishop, J. L., Ehlmann, B. L., Milliken, R. E., Wilhelm, M. B., et al. (2016). Orbital evidence for more widespread carbonate bearing rocks on Mars. *Journal of Geophysical Research: Planets*, *121*(4), 625–677. https://doi.org/10.1002/2015je004972

Yang, X.-Q., Kodikara, G. R. L., Luedeling, E., Yang, X.-F., He, J., Liu, P.-G., & Xu, J.-C. (2012). Looking below the ground: Prediction of Tuber Indicum habitat using the Weights of Evidence method. *Ecological Modelling*, *247*, 27–39. https://doi.org/10.1016/j.ecolmodel.2012.07.032

Zadeh, L. A. (1965). Fuzzy sets. *Information and Control*, *8*(3), 338–353. https://doi.org/10.1016/s0019-9958(65)90241-x

Zhao, J., Xiao, L., & Goudge, T. D. (2020). Paleolakes in the Northwest Hellas region, Mars: Implications for the regional geologic history and paleoclimate. *Journal of Geophysical Research: Planets*, *125*(3), e2019JE006196. https://doi.org/10.1029/2019JE006196

Zimmermann, H. J. (1991). *Fuzzy set theory and its applications* (Vol. 1). Springer.

Zimmermann, H. J., & Zysno, P. (1980). Latent connectives in human decision making. *Fuzzy Sets and Systems*, *4*(1), 37–51. https://doi.org/10.1016/0165-0114(80)90062-7

Zolotov, M. Y., & Mironenko, M. V. (2016). Chemical models for martian weathering profiles: Insights into formation of layered phyllosilicate and sulfate deposits. *Icarus*, *275*, 203–220. https://doi.org/10.1016/j.icarus.2016.04.011